Utrecht University

A comparison of GOCO05c satellite data to synthetic gravity fields computed from 3D density models in ASPECT

Master thesis by Wouter Janssen

July 2019

Abstract

One of the limitations of geodynamical modelling of the Earth's mantle nowadays is the absence of a reliable density model. This research uses scaled seismic tomography models in combination with crustal model CRUST1.0 to obtain a global density model. Through geodynamical finite element code ASPECT the gravity fields of these models are calculated and tested against the Earth's gravity field from satellite data (GOCO05c). Spectral filtering with spherical harmonics decomposition software is applied to investigate whether contributions from the Earth's mantle can be isolated. The long-wavelength gravity field obtained from CRUST1.0 seems to be a first-order estimate of the smooth parts of the Moho topography. However, including the mantle into the gravity models presents obstacles in the form of model resolution. Due to computational limitations, the gravity signals of the tomographic models do not completely converge. When merging crustal and tomographic data, the resolution of tomographic models prove insufficient in the upper part of the model and cause high-amplitude density jumps in the lithosphere. Neither the gravity signals of the tomographic models nor the gravity signals of the composite models correlate to GOCO05c in any spectral range. High-resolution topography of large density contrasts such as the lithosphere-astenosphere boundary, transition zone discontinuities and the CMB must be incorporated in order to achieve a more realistic gravity field and subsequently allow for the investigation of density perturbations in the mantle.

First supervisor: Dr. C. Thieulot
Second supervisor: Prof. Dr. W. Spakman

Key words:
Forward gravity modelling
ASPECT
Seismic tomography
CRUST1.0
Spherical harmonics

Contents

1 Introduction

1.1 Present-day tomography and the problem statement

At present, one of the major challenges on the front line of geodynamical modelling of the Earth is creating an accurate global model of density. Inciting all mass transport, from plate tectonics to mantle convection, this parameter bears importance. A density field of the Earth's mantle could serve as a stepping stone towards a complete mantle model including viscosity, temperature and rheology. However, owing to an obvious lack of observational data, constraints of density variations in the Earth's mantle and lower crust rely heavily on gravitational, seismological and mineralogical data. Generally, the methods employed to obtain a global density field are the scaling of temperature gradients (derived from lithospheric ages, e.g. Müller et al. (2008)) through the thermal expansivity coefficient (Bai et al. (2019); Chappell and Kusznir (2008); Oruç and Sönmez (2017)) and the direct scaling of wave speeds in seismic tomographic models (Bai et al. (2019); Deschamps et al. (2001); Karato and Karki (2001); Moulik and Ekström (2016); Simmons et al. (2010); Steinberger and Calderwood (2006)). In this thesis, the latter will be employed.

The technique of seismic tomography has been around for over 40 years (Dziewonski et al. (1977)) and it has developed into the primary source of insight regarding the Earth's deep interior. Tomographic imaging is the result of the inversion of large seismological data sets, consisting of arrival times, surface and body waveforms and free oscillations. Seismic tomography has succesfully allowed for the imaging of the deep earth and the identification of positive velocity anomalies (e.g. subducted lithosphere (Van der Hilst et al. (1997); van der Meer et al. (2018)) and negative velocity anomalies (e.g. Large Low Shear Velocity Provinces (Ritsema et al. (1998)).

Tomographic models exist in the form of relative seismic wave speeds perturbations, such as $\partial v_s/v_s(z)$ or $\partial v_p/v_p(z)$. However, the origin and the subsequent interpretation of these velocity anomalies remain controversial. Simple scaling factors are often being deployed in order to acquire a density field from wave speed perturbations (Bai et al. (2019); Ghosh et al. (2017)). Here, the assumption that velocity anomalies are to be linearly correlated to temperature anomalies and, consequently, to density perturbations (e.g. Bai et al. (2019); Ghosh et al. (2017)) is unfounded. Despite the fact that convolving these density perturbations with a 1D reference Earth model, in this case ak135 (Kennett et al. (1995)), may lead to a plausible density distribution, it would disregard potential compositional heterogeneity in the Earth's mantle. Here lies the crux of an ongoing debate: the contribution of compositional heterogeneity to the seismic signal is still largely unknown. State of the art studies present mounting evidence of a significant contribution of chemical heterogeneity (Koelemeijer et al. (2015); Moulik and Ekström (2016)). Also, chemical dissimilarities between ocean-island basalts (OIBs) and mid-ocean ridge basalt (MORBs) add to the paradigm of a non-uniform mantle composition.

Several studies suggest the ratios of shear V_s, compressional V_p and bulk sound V_ϕ velocity might provide constraints on the effect of chemical variation on seismic wave speed variations (Antolik et al. (2003); Kennett et al. (1998); Koelemeijer et al. (2015); Masters et al. (2000); Moulik and Ekström (2016); Simmons et al. (2010); Steinberger and Calderwood (2006); Su and Dziewonski (1997)). Investigation into these ratios consistently yield a negative correlation between bulk sound and shear velocities in the LLSVPs and their surrounding mantle; possible explanations being chemical heterogeneity or the presence of the phase transition from perovskite to post-perovskite. These depth-dependent scaling relations are based on mineral physics (Simmons et al. (2010); Steinberger and Calderwood (2006)) or the joint inversion of multiple seismic

data types in order to obtain independent constraints on wave speeds (Koelemeijer et al. (2015); Masters et al. (2000); Moulik and Ekström (2016); Simmons et al. (2010); Su and Dziewonski (1997)). Especially the recent addition of normal modes splitting data, or whole-earth oscillations, to the tomographic inversion process is convenient. Normal modes offer direct constraints on density variations, considering the gravitational force being the restoring force to the whole-earth oscillations. A limitation of this technique is the fact that their sensitivity is restricted to long wavelength structures (Moulik and Ekström (2016); Ritsema et al. (2011)).

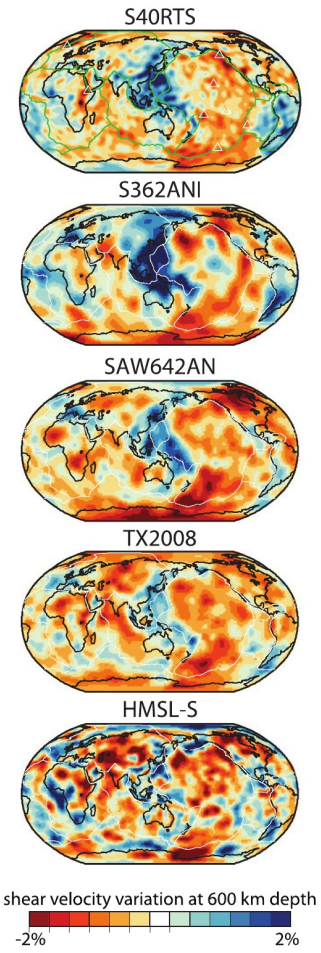

Figure 1: *A visual comparison of 5 shear wave tomography models, compiled by (Ritsema et al. (2011)) at 600km depth. The models showed are S40RTS (Ritsema et al. (2011)), S362ANI (Kustowski et al. (2008)), SAW642AN (Panning and Romanowicz (2006)), TX2008 (Simmons et al. (2009)) and HMSL-S (Houser et al. (2008)). Although the models show a general consensus, these models do not agree on amplitude and dimensions of the mantle structures.*

In the pursuit of a global density model, direct inversion of gravitational data is not feasible due to the inherent non-uniqueness of the solution. For instance, there is no way of distinguishing between a shallow positive density anomaly and a deeper heavier density anomaly; in theory they might produce identical gravity signatures (Zhou (2008)). However, forward gravity modelling could serve as a practical technique of validating tomographic models and their applied scaling parameters. Tomographic models are in need of validation because, although they are robust, they suffer from (a lesser degree of) non-uniqueness which is intrinsic to the inverse problem, even though regularization of the problem (i.e. truncation of spherical harmonics or any form of reduction of the model space) might provide a false feeling of a unique solution (Trampert (1998)). Despite the fact that numerous tomographic models show a general consensus, they do not unanimously agree on the amplitudes and wavelengths of anomalies (Ritsema et al. (2011)) (see figure 1).

Simultaneously, compared to other geophysical quantities, the gravity field and geoid are extremely well resolved nowadays (Steinberger and Calderwood (2006)). Calculating a synthetic gravitational signal of various tomographic models and quantitatively comparing it to the measured satellite gravity field might put constraints on scaling techniques, the visibility of deep anomalies, and the shape and wavelength of anomalies - which is the intent of this research. Two techniques will be applied: a numerical integration scheme and a spherical harmonics representation.

1.2 Computation of the gravitational field

The direct integration is conducted using the open-source geodynamical finite element code 'Advanced Solver for Problem in Earth's ConvecTion', version 2.0.1. (Heister et al. (2017)). ASPECT was initially developed to simulate thermally driven convection of highly viscous fluids, i.e. mantle convection. ASPECT is the preferred tool due to its parallelism, extensibility and especially the automatic mesh generation with two built-in mesh refinement features (see section 2). ASPECT has a built-in Navier-Stokes solver, meaning it solves for pressure, velocity and strain rate. This solver will not be applied in this thesis, yet it offers perspective on innovative research when applied on a satisfactory mantle density model. A satisfactory global density model can be used as a stepping stone towards a global viscosity field and subsequently, constraints on the rheology throughout the entire mantle. Although calculating gravity fields by direct integration is computationally expensive compared to spherical harmonics methods (Root et al. (2016)), ASPECT offers a suitable platform whilst working towards this complete model of the Earth's mantle by facilitating further development of the models. Variability of time can be introduced by solving the Stokes equation, simulating mantle convection and allowing for the generation of surface movement. When compared to accurate GPS-data, surface movement provides additional valuable constraints on the dynamics of the mantle. Moreover, obtaining an accurate global model of the Earth's mantle allows for the addition of geodynamical processes such as subduction zones or mid-ocean ridges; making inspection from a complete and heterogeneous mantle perspective feasible, as opposed to a confined box perspective with its accessory limitations such as edge effects (Chertova et al. (2012)).

For benchmarking and filtering purposes, additional gravity fields calculations are performed using a spherical harmonics representation. The software, provided by Root et al. (2016), is based on a 'Fast Spectral Method' (FSM) and uses a binomial series expansion to solve the volume integral. As the name implies, this method is computationally efficient, in contrast to numerical integration. Numerical integration is computationally expensive because for every sampled point, the total gravitational signal is the sum of the gravitational signal of each individual mesh cell. Besides being computationally more efficient, the spherical harmonics-based approach also allows for depth-varying compositional layers, whereas ASPECT employs layers in the form of spherical shells.
The spherical harmonics software is especially convenient as it allows for spectral filtering in the form of spherical harmonics coefficients. Filtering can be applied to any scalar field, therefore also any results computed with ASPECT. Thus, gravity scalar fields can be decomposed spectrally to remove specific wavelengths from the signal. Under the postulation long-wavelength spectrum is generated by mantle structures, this is a powerful tool to separate the gravitational signals of deep and shallow sources.
Draw-backs of the spherical harmonics method is an error (albeit a minor one) introduced by the approximation of the geometry of mass layers (Root et al. (2016)). Moreover, the spherical harmonics software is capped at a maximum degree and order (d/o) 179, corresponding to a maximum resolution of $\sim 1^{\circ}$ (see section 2).

Lower mantle density contrasts produce the largest wavelengths in the gravitational signal (d/o 2-3) (Bowin (1986); Hager et al. (1985)); this was already established by a spherical harmonics representation of the earliest tomographic models. Hager et al. (1985) referred to the correlation of their model of density contrasts in the lower mantle of degree 2-3 (a resolution of $\sim$ 6600 km) to the longest-wavelength component of the geoid as being "embarrassingly good", but confessed not finding any correlation with a model of degree ≥ 4. Also, mantle convection will produce gravitational signatures in the range of thousands of kilometers (Sebera et al. (2018)). Case studies on both continental and oceanic lithosphere

suggest density perturbations in the upper mantle would produce medium wavelength gravity signals (d/o $\geq$ 10) (Kaban et al. (2002); Sobolev et al. (1997); Tenzer et al. (2015b)). Kuhn and Featherstone (2005) suggest upper and middle mantle anomalies contribute to gravity perturbations in the spectral range d/o 6-100. For smaller wavelengths (down to 100 km (Sebera et al. (2018)), the gravitational signal is characterized by isostasy and the flexural response of the plate. In this case, the Bouguer anomaly (the free-air anomaly corrected for elevation above the reference sphere) correlates to the wavelength of the topography (Simons et al. (2000)). At even smaller wavelengths, below 100 km, the lithosphere is rigid enough to support the topography (Forsyth (1985); Sebera et al. (2018)). Consequently, at the high-frequency spectrum free-air gravity anomalies correlate directly with the topographic load.

Forward gravity modelling has nowadays become feasible partially due to the availability of high-resolution of satellite data. The GOCE mission ('Gravity Field and Steady-State Ocean Circulation Explorer') was launched in 2009 carrying a new instrument for gravity measurements (Bouman et al. (2011); Fullea et al. (2015); Xu et al. (2017)). This instrument, called the three-axis gradiometer, measures gravity perturbations in three spatial directions. Gravity gradient tensor data from this instrument has increased sensitivity to edges and center of mass of a gravity anomaly, thus recovering a sharper image where conventional gravity data would show a diffused image (Dubey and Tiwari (2016)). The three-axis gradiometer is accurate to $\pm$10 cm and $\pm$3 mgal for geoid and gravity anomalies respectively, and a resolution of around 90 km (degree and order 220) (Pail et al. (2013)). Numerous studies have employed GOCE gravity gradients to scrutinize the Earth's crust and oceans and, moreover, recent studies exploit these gradients to image subsurface mass anomalies. For instance, Fullea et al. (2015) imaged the Alboran slab using GOCO03s and Guy et al. (2017) constrains the Moho topography beneath the Central Asian Orogenic Belt using GOCE-only data set EGM_TIM_RL0.

1.3 Overview of utilized data sets

This research utilizes a number of different data sets which, in turn, differ in terms of data range, data resolution and physical quantity. An overview is given in table 1:

Table 1: Overview of utilized data sets in this research.

Data set	**Physical quantity**	**Resolution**	**Range (radius)**	**Type data**
CRUST1.0	ρ (kg/m^3)	$1^\circ \times 1^\circ \times$ 100 m	6291-6377 km	Crustal compilation
ak135	ρ (kg/m^3)	$\sim$ 43km	3571 - 6371 km	Travel time tables
P06-CSloc	δlnVp (%)	$0.5^\circ \times 0.5^\circ \times$ 10km	3571-6371 km	Tomography
P06-3Dloc	δlnVp (%)	$0.5^\circ \times 0.5^\circ \times$ 10km	3571-6371 km	Tomography
SL2013+S40RTS	δlnVs (%)	$0.5^\circ \times 0.5^\circ \times$ 10km	3571-6371 km	Tomography
GOCO05c	Gravity (mgal)	$15' \times 15'$	N/A	Satellite

1.3.1 CRUST1.0

The crustal data set CRUST1.0 (Laske et al. (2013)) is a compilation of numerous sedimentary models in combination with seismic data. Its predecessor, 'A Global Digital Map of Sediment Thickness' (Laske and Master (1997)) is digitalization of 12 sedimentary thickness maps. CRUST1.0 has a resolution of $1^\circ \times 1^\circ$ and includes topography, bathymetry and ice cover. Vertically it consists of distinct compositional layers, being: ice, water, three sedimentary layers layers and upper, middle and lower crystalline crust. Cells lacking data coverage have been assigned crustal thickness by extrapolation.

1.3.2 ak135

The one-dimensional data set ak135 (Kennett et al. (1995)) is constructed from a wide range of seismic travel time tables and offer a radially stratified velocity and density profile of the Earth (including the core) (see figure 2). It is an updated version of travel time model iasp91 (Kennett and Engdahl (1991)) and uses more seismic data than the Preliminary Reference Earth Model (PREM) (Dziewonski and Anderson (1981)), although deviations between the two are minor and mostly reside in the core. Amaru (2007) employs ak135 as a reference density profile for the wave speed perturbations of the tomographic model described below (P06-3Dloc, P06-CSloc, SL2013+S40RTS).

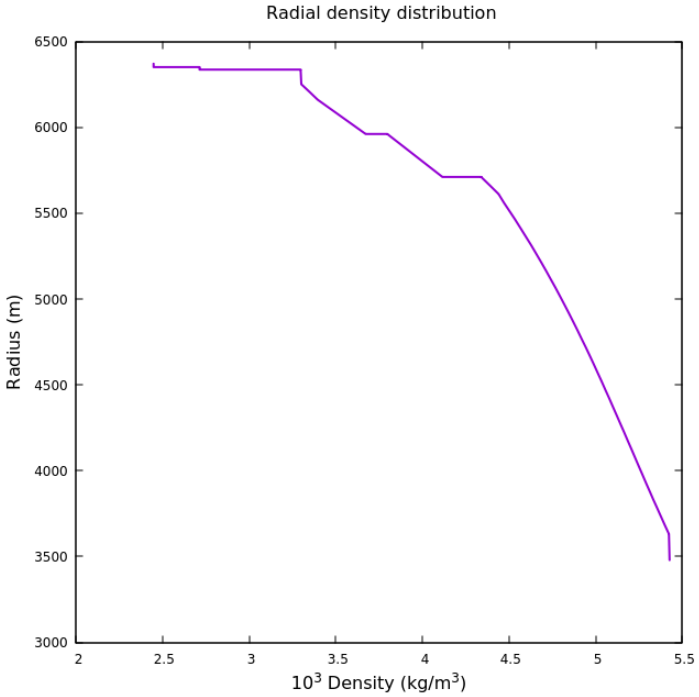

Figure 2: *Radial density profile ak135 (Kennett et al. (1995))*

1.3.3 P06-CSloc

The tomographic model P06-CSloc (Amaru (2007)) uses a combination of tomographic models S20RTS (Ritsema et al. (1999)) and CUB2.0 (Ritzwoller et al. (2003)) as a 3D reference model. CUB2.0 is based on surface wave group and phase velocities and is most sensitive to the shallower regions. CUB2.0 utilizes crustal model CRUST2.0 (Bassin and Masters (2000)), predecessor to CRUST1.0, as reference model. In contrast, S20RTS is based on Rayleigh wave phase velocities, V_s travel times and normal mode splitting functions. Between 200 and 300 kilometers depth, the reference models are conjoined using a depth-weighted average of both models (Amaru (2007)).
P06-CSloc has a lateral resolution of $1° \times 1°$ and radially of 10 kilometers and spans from the surface to the CMB. This data set gives wave speed perturbations with respect to the one-dimensional reference model ak135 (Kennett et al. (1995)).

1.3.4 P06-3Dloc

Similar to P06-CSloc, the tomographic model P06-3Dloc (Amaru (2007)) uses a combination of tomographic models S20RTS and CUB2.0 and $P06^+$ as a 3D reference model. $P06^+$ is added in order to enhance amplitudes in lesser resolved

areas. The systematic underestimation of velocity amplitudes during the inversion process is a result of, for instance, the incomplete convergence of the least-squares algorithm, poor resolution or regularization (Amaru (2007)).
Identical to P06-CSloc, P06-3Dloc has a resolution laterally of $1° \times 1°$ and radially of 10 kilometers and spans from the surface to the CMB. This data set also gives wave speed perturbations with respect to the one-dimensional reference model ak135 (Kennett et al. (1995)).

1.3.5 SL2013+S40RTS

The tomographic data set SL2013+S40RTS is a combination of S40RTS (Ritsema et al. (2011)) and SL2013 (Schaeffer and Lebedev (2013)). SL2013 is based on a combination of body and surface waves and ranges from the surface to the 660 km seismic discontinuity. Supplementary, S40RTS is based on Rayleigh wave phase velocities, V_s body wave travel times and normal mode splitting functions, similar to its predecessor S20RTS. In constrast to SL2013, S40RTS spans from the surface down to the CMB.
In agreement with the P06-data, SL2013+S40RTS has a resolution laterally of $1° \times 1°$ and radially of 10 kilometers and spans from the surface to the CMB. The data set gives wave speed perturbations with respect to the one-dimensional reference model ak135 (Kennett et al. (1995)).

1.3.6 GOCO05c

For the purpose of (spectral) comparison, satellite data from GOCO05c (figure 3) will be utilized for this research (Fecher et al. (2017)). The data set is a compilation of gravity anomaly field data from GRACE, GOCE, altimetry and terrestrial measurements. GOCO05c is currently one of the most up-to-date data sets freely available. It combines mostly gravity data of missions GRACE ('Gravity Recovery And Climate Experiment') and the new GOCE mission, which complement one another spectrally. GOCO05c is resolved to d/o 3-720 and thus a spatial resolution of $15' \times 15'$. The largest component of the data is the satellite-only GOCO05s (not to be confused with GOCO05c) which is resolved up d/o 280 and consists of data originating from the GRACE and GOCE mission combined with LEOs (Low Earth Orbiting satellites) and SLR (Satellite Laser Ranging). GOCO05c is an improvement to GOCO05s for it is supplemented with data from satellite radar altimetry (e.g. DTU2013 with $1' \times 1'$ (Andersen et al. (2010))).

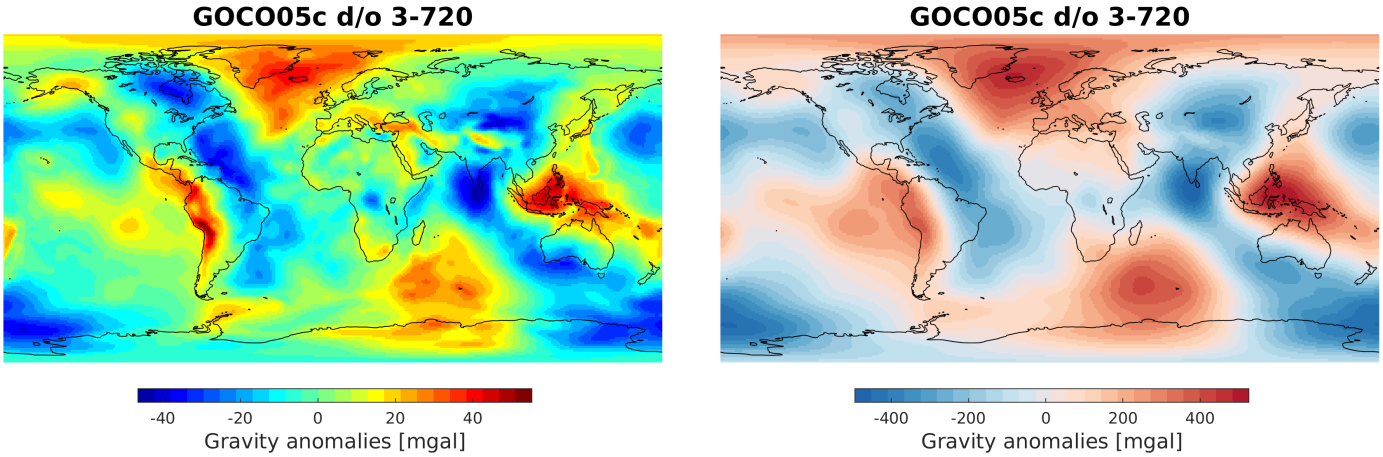

Figure 3: *a) The gravity anomaly field of d/o 3-720 from the GOCO05c data set. b) The gravity potential field from the same data set.*

2 Methodology

2.1 Gravity

In this research, relevant quantities are the gravitational potential V, the gravity vector $\vec{g}$, the gravity anomaly and the gravity gradient tensor.
The expression for a gravitational potential field V is:

$$V(R) = -\frac{GM}{R} \tag{1}$$

where G is the gravitational constant, M is the mass inducing the gravity field and R is the distance between the measurement point and the center of mass.
The gravity vector in a Cartesian system is computed by taking the first spatial derivative in the radial direction:

$$\frac{\partial V}{\partial z} = \frac{GM}{R^2}\frac{\partial R}{\partial z} = g \tag{2}$$

The gravity anomaly is the perturbation of the gravitational signal with respect to its background value. This process of subtracting the background gravity field is different for the direct integration and spherical harmonics method (see section 2.2 and 2.3). To ensure these quantities match, the values of the background gravity signal have been benchmarked (see section 4).

2.2 ASPECT

Disclaimer: this research uses pre-Hackathon (May 2019) software only. This version of ASPECT does not allow for pre-refinement mesh handling, nor refine in a specificable lateral range. For a spherical shell geometry, the mesh can only be modified through 'General Mesh Refinement', 'Adaptive Mesh Refinement' and 'Minimum Refinement Technique' features. Since the time of writing, ASPECT's mesh refinement techniques have been improved.

The 3D model in ASPECT consists of a sphere with an internal density distribution. These density distributions are in the form of (scaled) tomography and crustal models, or a combination thereof. No temperature and viscosity profiles will be imposed. For simplicity, the Earth's core is omitted. The model will not be time dependent and will not accommodate movement of material. ASPECT demands a laterally regular grid, confining the spherical model to be composed of spherical shells. These spherical shells are allowed to differ in thickness. Any models with variable layer thickness (e.g. CRUST1.0) are projected on this mesh of spherical shells. Topography is resolved by adding 'sticky-air' of negligible density to the nodes adjacent to it.

ASPECT utilizes the *dealii* library for the finite element mesh handling and the *p4est* library for parallel mesh handling. The automatically generated spherical mesh consists of irregular hexahedra and is controlled through General Mesh Refinement (GMR) and Adaptive Mesh Refinement (AMR). One refinement level in ASPECT comprises of subdivision into 8 cells. The amount of mesh cells for the first 8 levels of GMR are given in table 2. GMR refines the entire domain, whereas AMR refines for large contrasts on specified properties. Spherical shell geometries can be refined locally for specifiable radii (the so-called Minimum Refinement Function), yet do not offer constraints on the spatial distribution of

mesh cells before initial refinement. This is possible when using a spherical chunk geometry. For more on ASPECT, see `https://aspect.geodynamics.org`

Level of GMR	Number of cells	Lateral resolution (deg)	Lateral resolution (km)	Radial resolution
1	96	180°× 90°	20015 km × 10007 km	1400 km
2	768	90°× 45°	10007 × 5004 km	700 km
3	6,144	45°× 22.5°	5004 km × 2502 km	350 km
4	49,152	22.5°× 11.25°	2502 km × 1251 km	175 km
5	393,216	11.25°× 5.625°	1251 km × 625 km	87.5 km
6	3,145,728	5.625°× 2.813°	625 km × 313 km	43.75 km
7	25,165,824	2.813°× 1.406°	313 km × 156 km	21.875 km
8	201,326,592	1.406°× 0.703°	156 km × 78 km	10.938 km

Table 2: The amount of mesh cells per level of GMR and the corresponding model resolution. The radial resolution is given in the form: [lon × lat].

Numerical integration is performed through Gauss-Legendre Quadrature (GLQ). This numerical integration scheme comprises a summation of specific weighted values. The general form of GLQ states:

$$\int_{-1}^{+1} f(x)dx = \sum_{i=1}^{n} w_i f(x_i) \tag{3}$$

in which points x_i represent the roots (intersection with horizontal axis) of Legendre polynomials P_n. Legendre polynomials are a set of orthogonal polynomials of ascending degree. Fortunately, GLQ guarantees exact results for polynomials of order $2n-1$. When functions contain singularities they can not be approximated by polynomials and their integration is inaccurate.

To obtain the gravitational field from the density distribution, the following integral is employed:

$$g(r) = G \iiint_V \frac{\rho(r')}{|r-r'|^3}(r-r')dr' \tag{4}$$

in which $G = 6.67408 \times 10^{-11}\ kg^{-1}m^3s^{-2}$ is the gravitational constant, $\rho(r')$ is the density distribution per volume element and $|r-r'| = \sqrt{(x-x')^2+(y-y')^2+(z-z')^2}$ is the distance between the point of measurement and nodal point.

Computation of this integral, using Gauss-Legendre quadrature methodology, is performed according:

$$g = G \sum_{e=1}^{N_{ele}} \sum_{i=1}^{N_{GLQ}} \sum_{j=1}^{N_{GLQ}} \sum_{k=1}^{N_{GLQ}} \frac{\rho(r_{ijk})}{|r-r_{ijk}|^3}(r-r_{ijk})|J_e|\omega_i\omega_j\omega_k \tag{5}$$

in which the ω-variables are the weighing factors and $|J_e|$ is the determinant of the Jacobian operator.

The integration kernel of equation (5) is not a polynomial. In combination with GLQ, this potentially introduces an unknown error in ASPECT's numerical integration when using a mesh consisting of irregular hexahedra. In order to investigate this error, the gravitational signal of a uniform sphere is benchmarked against the analytical gravity value of the sphere (see section 3).

The default number of quadrature points, per 3D mesh cell, is 2 per spatial direction or $2^3 = 8$ quadrature points. When integrating the model in order to obtain the gravitational field, ASPECT offers an option to increase the quadrature points per mesh cell. For example, adding another 3 levels of quadrature points would yield a total amount of quadrature of $2^6 = 64$. The effect of an increase in quadrature points on the gravitational signal is demonstrated in section 3.

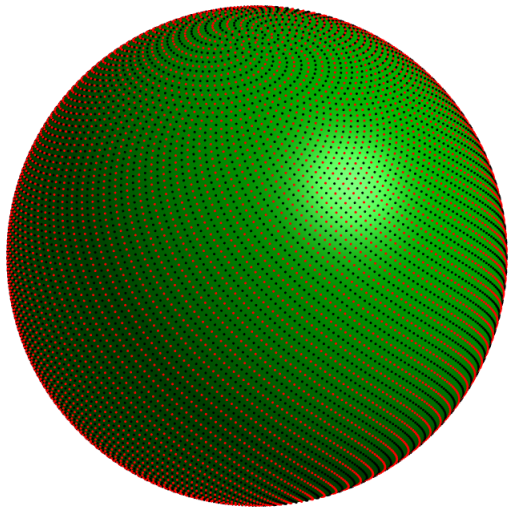

Figure 4: *The 16,000 sampling positions of the satellite when re-sampling the gravity field, in order to improve the mean value.*

The synthetic gravity signal of the models in ASPECT will be calculated at a distance of 225 km (similar to GOCEs orbit) above the surface of the model. The gravity anomalies are calculated by subtracting the mean gravity field. The sampling will be performed in an equiangular fashion, as is intrinsic to ASPECT. Equiangular sampling does not mean equidistant sampling on a sphere and oversampling of the poles might result in an underestimation of the mean gravity signal of the model. Consequently, this would shift the gravity anomalies. In order to compensate for this oversampling at the poles, and the subsequent inaccurate mean of the gravity field, the gravity field is re-sampled. Figure 4 shows the sampling 'trajectory' of the satellite, being a spiralling motion over a sphere. The new calculation of the mean is based on 16,000 measurements and yields a representative mean of the gravity signal, in turn, leading to an improved gravity anomaly field. The number of measurements is chosen such that equatorial mesh cells don't get sampled more than once. The effect of re-sampling the gravity fields is demonstrated in section 3.

2.3 Spherical harmonics

The spherical harmonics software of Root et al. (2016) uses a fast spectral method to evaluate the volume integral of the gravity calculation. This software employs a spherical harmonics expansion to constrain the gravitational potential. This subsection provides the theoretical background on which this software operates, which is largely based on Heiskanen and Moritz (1967) and Novák and Grafarend (2006).

Harmonics functions are functions that satisfy Laplace's equation ($\Delta V = 0$) in every point within their domain. The most common harmonic function is the reciprocal distance between the points (x, y, z) and (x_0, y_0, z_0):

$$\frac{1}{r} = \frac{1}{\sqrt{(x-x_0)^2 + (y-y_0)^2 + (z-z_0)^2}} \tag{6}$$

The formula for gravitational potential V is characterized by this reciprocal distance kernel and therefore qualifies as an harmonic function. The solution to harmonic functions can be approximated using a spherical harmonics expansion, which is demonstrated below.

Spherical harmonic functions satisfy the Laplace's equation in a spherical coordinate system (r, θ, ϕ):

$$\Delta V \equiv \frac{\partial^2 V}{\partial r^2} + \frac{2}{r}\frac{\partial V}{\partial r} + \frac{1}{r^2}\frac{\partial^2 V}{\partial \theta^2} + \frac{\cos(\theta)}{r^2 \sin(\theta)}\frac{\partial V}{\partial \theta} + \frac{1}{r^2 \sin^2(\theta)}\frac{\partial^2 V}{\partial \phi^2} = 0 \tag{7}$$

in which no terms with products of dr, $d\theta$ and $d\phi$ exist because of the orthogonality between these coordinates.
The solutions to Laplace's equation in spherical coordinates is constructed by taking a trial substitution in which the radial and lateral coordinates are separated:

$$V(r, \theta, \phi) = f(r)Y(\theta, \phi) \tag{8}$$

$$\Delta V = \frac{1}{f}\Big(r^2\frac{\partial^2 f}{\partial r^2} + 2r\frac{\partial f}{\partial r}\Big) + \frac{1}{Y}\Big(\frac{\partial^2 Y}{\partial \theta^2} + \frac{\cos(\theta)}{\sin(\theta)}\frac{\partial Y}{\partial \theta} + \frac{1}{\sin^2(\theta)}\frac{\partial^2 Y}{\partial \phi^2}\Big) = 0 \tag{9}$$

As a result of the separation of the radial and lateral variables, both terms must be constant and can be evaluated separately. In order to obtain the most convenient solutions, the constant is chosen to be $n(n+1)$ for $n \in \mathbb{N}$:

$$\frac{1}{f}\Big(r^2\frac{\partial^2 f}{\partial r^2} + 2r\frac{\partial f}{\partial r}\Big) = n(n+1) \tag{10}$$

$$\frac{1}{Y}\Big(\frac{\partial^2 Y}{\partial \theta^2} + \frac{\cos(\theta)}{\sin(\theta)}\frac{\partial Y}{\partial \theta} + \frac{1}{\sin^2(\theta)}\frac{\partial^2 Y}{\partial \phi^2}\Big) = n(n+1) \tag{11}$$

If a differential operator is linear, the sum between solutions also yields a solution to a PDE. Solving equation (10) gives two solutions:

$$f(r) = Ar^n + Br^{-(n+1)} \tag{12}$$

where A and B are arbitrary integers.
These solutions are called 'solid spherical harmonics' and will be evaluated separately henceforth. From equation (12),

the preliminary solutions are:

$$V = \sum_{n=0}^{\infty} r^n Y_n(\theta, \phi) \tag{13}$$

$$V = \sum_{n=0}^{\infty} \frac{Y_n(\theta, \phi)}{r^{n+1}} \tag{14}$$

Now, solving for the 'surface spherical harmonics' $Y_n(\theta, \phi)$ is done in a similar fashion, through a trial substitution:

$$Y_n(\theta, \phi) = g(\theta)h(\phi) \tag{15}$$

Substituting into equation (11):

$$\frac{\sin(\theta)}{g}\Big(\sin(\theta)\frac{d^2g}{d\theta^2} + \cos(\theta)\frac{dg}{d\theta} + n(n+1)\sin(\theta)g\Big) = -\frac{1}{h}\frac{d^2h}{d\phi^2} \tag{16}$$

Again, since both sides have dependencies on different variables and can be seperately evaluated against a constant. The constant is a positive integer and is denoted as m^2 for $m \in \mathbb{Z}$.

$$\frac{\sin(\theta)}{g}\Big(\sin(\theta)\frac{d^2g}{d\theta^2} + \cos(\theta)\frac{dg}{d\theta} + n(n+1)\sin(\theta)g\Big) = m^2 \tag{17}$$

$$-\frac{1}{h}\frac{d^2h}{d\phi^2} = m^2 \tag{18}$$

The solution to equation (18) is:

$$h(\phi) = A\cos(m\phi) + B\sin(m\phi) \tag{19}$$

where A and B are arbitrary integers.
The solution to equation (17), however, is more complicated and coincides with Legendre polynomials P of degree n and order m.

$$g(\theta) = P_{nm}(\cos(\theta)) \tag{20}$$

The solution for surface spherical harmonic Y_{nm} is a linear combination of these solutions:

$$Y_n(\theta, \phi) = \sum_{m=0}^{n} \Big[a_{nm}P_{nm}(\cos(\theta))\cos(m\phi) + b_{nm}P_{nm}(\cos(\theta))\sin(m\phi)\Big] \tag{21}$$

in which a and b are arbitrary constants.
Subsequently:

$$V_1(r, \theta, \phi) = \sum_{n=0}^{\infty} r^n \sum_{m=0}^{n} \Big[a_{nm}P_{nm}(\cos(\theta))\cos(m\phi) + b_{nm}P_{nm}(\cos(\theta))\sin(m\phi)\Big] \tag{22}$$

$$V_2(r,\theta,\phi) = \sum_{n=0}^{\infty} \frac{1}{r^{n+1}} \sum_{m=0}^{n} \Big[a_{nm} P_{nm}(\cos(\theta)) \cos(m\phi) + b_{nm} P_{nm}(\cos(\theta)) \sin(m\phi) \Big] \tag{23}$$

which is the general expression for spherical harmonics. Specifically, equation (23) evaluates the gravitational potential field V outside a certain sphere and equation (22) evaluates the potential field within the sphere. This can be deducted from the first summation term; the gravitational potential increases with r inside the sphere and decreases with r outside the sphere.

When defining a satellite location (r,θ,ϕ) outside the sphere and an infinitesimal volume element at location (r',θ',ϕ') within the shere, this specific software employs a spherical harmonic representation of the inverse distance kernel which looks like:

$$\frac{1}{l} = \mathcal{L}^{-1}(r,\theta,\phi,r',\theta',\phi') = \sum_{n=0}^{\infty} \sum_{m=-n}^{n} \Big(\frac{r'^n}{r^{n+1}} \Big) \Big(\frac{1}{2n+1} \Big) Y_{nm}(\theta,\phi) Y_{nm}^*(\theta',\phi') \tag{24}$$

where Y_{nm} and Y_{nm}^* are normalized versions of equation (21) which simplify the constants a and b to be $(2n+1)^{-1}$.

Thus, when computing the gravitational potential of a spherical shell of constant density between radial coordinates r_{upper} and r_{lower}, the expression becomes:

$$\begin{aligned} V(r,\theta,\phi) &= G \int_{\phi'=0}^{2\pi} \int_{\theta'=0}^{\pi} \int_{r'=r_{lower}(\theta',\phi')}^{r_{upper}(\theta',\phi')} \rho(r',\theta',\phi') \mathcal{L}^{-1}(r,\theta,\phi,r',\theta',\phi') r'^2 \sin(\theta') d\theta' d\phi' \\ &= \sum_{n=0}^{\infty} \sum_{m=-n}^{n} \Big(\frac{1}{r} \Big)^{n+1} \frac{1}{2n+1} Y_{nm}(\theta,\phi) \int_{\phi'=0}^{2\pi} \int_{\theta'=0}^{\pi} \rho(\theta',\phi') Y_{nm}^*(\theta',\phi') \int_{r'=r_{lower}(\theta',\phi')}^{r_{upper}(\theta',\phi')} r'^{n+2} dr' \end{aligned} \tag{25}$$

which can be rewritten in terms of a deviation from a reference sphere R by substituting $r_{upper}(\theta',\phi') = R + U(\theta',\phi')$ and $r_{lower}(\theta',\phi') = R + L(\theta',\phi')$:

$$\int_{r'=r_{lower}(\theta',\phi')}^{r_{upper}(\theta',\phi')} r'^{n+2} dr' = \frac{1}{n+3} \Big([R + U(\theta',\phi']^{n+3} - [R + L(\theta',\phi']^{n+3} \Big) \tag{26}$$

This integral is approximated by means of binomial series expansion after replacing U and L with their normalized values (i.e. $\hat{U} = U/R$ and $\hat{L} = L/R$) and $\nu = n+3$.

$$\begin{aligned} \frac{1}{\nu} \Big[(R+U)^\nu - (R+L)^\nu \Big] &= \frac{R^\nu}{\nu} \sum_{k=0}^{\nu} \binom{\nu}{k} \Big[\hat{U}^k - \hat{L}^k \Big] \\ &= \frac{R^\nu}{\nu} \sum_{k=0}^{\alpha} \binom{\nu}{k} \Big[\hat{U}^k - \hat{L}^k \Big] + \epsilon_\alpha \\ &= \frac{R^{n+3}}{n+3} F(\theta',\phi') \end{aligned} \tag{27}$$

where α is the truncation value of the binomial series expansion and ϵ_α is the error introduced by this truncation.

Substituting this into (25) gives:

$$V(r,\theta,\phi) = GR^2 \sum_{n=0}^{\infty} \sum_{m=-n}^{n} \Big(\frac{R}{r} \Big)^{n+1} \frac{1}{(2n+1)(n+3)} Y_{nm}(\theta,\phi) \int_{\phi'=0}^{2\pi} \int_{\theta'=0}^{\pi} \rho(\theta',\phi') F(\theta',\phi') Y_{nm}^*(\theta',\phi') d\theta' d\phi' \tag{28}$$

Now, so-called global spherical harmonics analyses (GSHA) is performed on the multiplication of the density distribution

and the function F:

$$\rho(\theta',\phi')F(\theta',\phi') = \sum_{n=0}^{\infty}\sum_{m=-n}^{n} C_{nm}Y_{nm}(\theta',\phi') \tag{29}$$

Substitute into equation (28):

$$V(r,\theta,\phi) = GR^2\sum_{n=0}^{\infty}\sum_{m=-n}^{n}\left(\frac{R}{r}\right)^{n+1}\frac{1}{(2n+1)(n+3)}Y_{nm}(\theta,\phi)\times\sum_{n'=0}^{\infty}\sum_{m'=-n'}^{n'}C_{n'm'}\int_{\phi'=0}^{2\pi}\int_{\theta'=0}^{\pi}Y_{n'm'}(\theta',\phi')Y^{*}_{nm}(\theta',\phi')d\theta' d\phi \tag{30}$$

However, due to the inherent orthogonality between the fully normalized Legendre's function for $n \neq m$, the integral over the product between two Legendre functions is always equal to a constant:

$$\iint_{\sigma} Y_{nm}^2\, d\sigma = 4\pi \tag{31}$$

where σ denotes an arbitrary surface element of a sphere.
Subsequently, the eventual expression for the gravitational potential is:

$$V(r,\theta,\phi) = GR^2\sum_{n=0}^{\infty}\sum_{m=-n}^{n}\left(\frac{R}{r}\right)^{n+1}\frac{4\pi}{(2n+1)(n+3)}C_{nm}Y_{nm}(\theta,\phi) \tag{32}$$

The final step of the derivation comprises of a division by the reference M, in the form of $M = \frac{4}{3}\pi\rho_{earth}R^3$, where ρ_{earth} denotes the Earth's average density.

$$V(r,\theta,\phi) = \frac{GM}{R}\sum_{n=0}^{\infty}\sum_{m=-n}^{n}\left(\frac{R}{r}\right)^{n+1}\frac{3}{(2n+1)(n+3)}\frac{1}{\rho_{earth}}C_{nm}Y_{nm}(\theta,\phi) \tag{33}$$

The 'fast spectral method', as derived above, is prone to significant errors for deeper mass layers (e.g. mantle) as a result of the truncation of the binomial series expansion. By introducing a depth-dependent reference sphere R whilst computing the spherical harmonics coefficients and back-projecting to the original sphere before synthesizing the gravitational signal, these errors are largely eliminated. This software is computationally fast and yields an accuracy of ± 1 mgal for a truncation value of $\alpha = 3$. The main draw-back being that there is no room for resolution improvement without increasing the truncation in order to fulfil the convergence criterion.

The software is subdivided into a routine performing the spherical harmonics analysis and another one performing spherical harmonics synthesis. This subdivision is especially practical, for it allows us to decompose scalar fields computed by ASPECT and re-synthesize for a specified spectral range. In spherical harmonics theory, the zeroth degree and order approximation represents a spheroid and the first degree and order approximation represents an ellipsoid. As an alternative to subtracting a mean gravity field to obtain a gravity anomaly field, the first spherical harmonics can be omitted. The synthetic model is spherical and therefore only the first spherical harmonics coefficient must be omitted. Satellite data omits the first 3 spherical harmonics coefficients, for it has to approximate an oblate spheroid geometry.

3 Results

3.1 Benchmarks

3.1.1 Uniform spherical shell

In order to accurately constrain potential errors in the gravitational signal introduced by, for example, the mesh or the calculation of the background gravity field, resolution tests have been performed on a uniform sphere of constant density in ASPECT. This approach allows a quantitative comparison to an analytical solution. The benchmark is performed using a sphere of constant $\rho = 5513\text{kg}^{-3}$, which is the average density of the Earth. The mesh is refined step-by-step by incrementing the GMR by 1, starting with a minimum of 12 mesh cells (see Table 2).
The analytical solution for the gravity vector above a spherical shell is:

$$g = \frac{GM}{R_{sat}^2} = \frac{4G\pi\rho}{3R_{Sat}^2}(r_{outer}^3 - r_{inner}^3) = 7.5475\text{ms}^{-2} \tag{34}$$

where $G = 6.67408 \times 10^{-11}$ m^3 kg^{-1} s^{-2} is the universal gravitational constant, ρ is a uniform density of 5513 kgm^{-3}, r_{inner} and r_{outer} are the radii of the spherical shell (3571 and 6371 km, resp.) and R_{sat} is the radius plus the satellite height (6596 km).

The uniform spherical shell benchmark was sampled at a 225 km altitude above the model (similar to GOCE) and at a $1^\circ \times 1^\circ$ interval, which is the lateral resolution of the data utilized in this research.
Figure 5 reveals an influence of the mesh resolution on the gravity fields, in the form of a checkerboard pattern indicative of the nodal points. The influence of the mesh resolution decreases rapidly with refinement. All scalar fields show a consistent overestimation of the gravity vector in 8 points, which coincide with a junction of mesh cells.
The highest achievable resolution, in terms of memory, is a mesh with a refinement of GMR=8 accompanied by a quadrature degree increase ($2^6 = 64$ points, as opposed to the default $2^3 = 8$ points). This increase in quadrature points, although computationally expensive ($\sim$9 hours on 960 cores), eradicates all effects of the mesh resolution and yields in a minimal error of $\sim 1.155 \times 10^{-6}$ mgal introduced by the geometry of the irregular hexahedra (figure 6).
The gravity converges to a gravity vector of 7.54729ms^{-2}, meaning there is a 21 mgal error between the benchmark and the analytical solution (7.54750ms^{-2}). This error is likely to be caused by the integration kernel not being a polynomial.

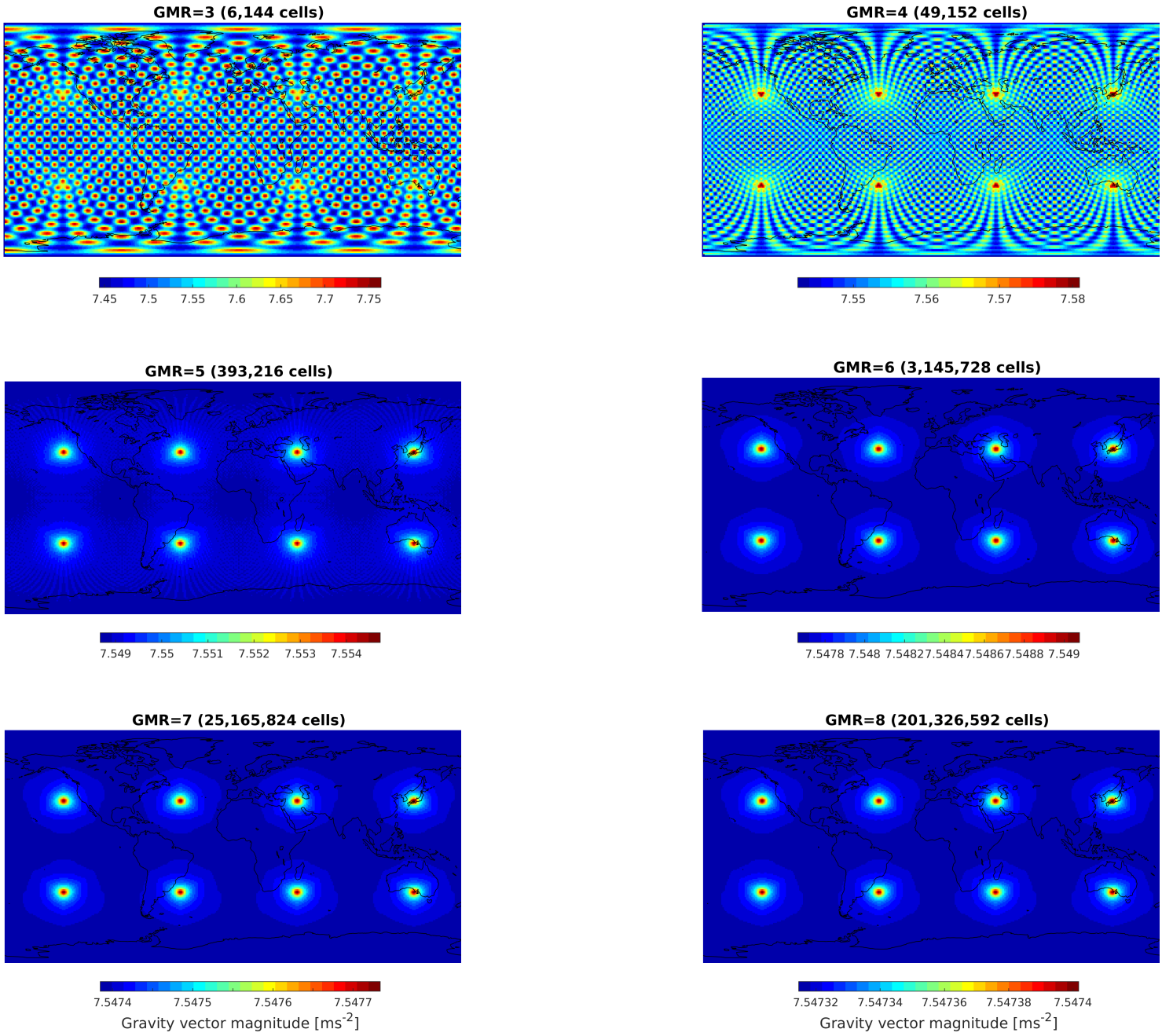

Figure 5: *The vertical gravity vector for the uniform spherical shell benchmark from GMR = 3 (top left) to GMR = 8 (bottom right).*

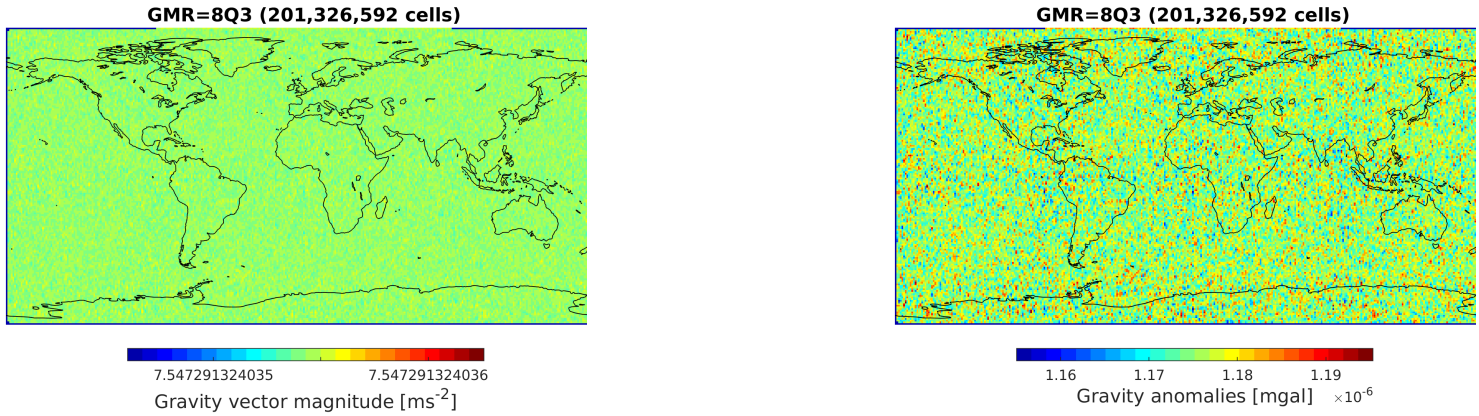

Figure 6: *a) The vertical gravity vector and b) the gravity anomalies for GMR = 8, where the gravity calculation was performed using 64 quadrature points (as opposed to 8).*

3.1.2 Uniform chunk

Aforementioned, the spherical shell geometry intrinsic to ASPECT does not allow a control of the original mesh before initial refinement. Consequently, GMR refines the mesh equally in every spatial direction. Yet, data set CRUST1.0 has a lateral resolution of $1^\circ \times 1^\circ$ and a radial resolution of 10 meters. This means that, for a spherical shell geometry, improving the radial resolution leads to severe lateral oversampling. The spherical chunk geometry allows for the modification of the pre-refinement mesh. A benchmark was performed on a hollow hemisphere of constant density ($\rho = 1000$ kgm^{-3}), with a longitude and latitude both ranging from $[-89.99^\circ : 89.99^\circ]$.

The approximate analytical solution to this problem is:

$$\vec{g} = \frac{G\rho}{r_{sat}^2}\iiint_V 1dV = \frac{G\rho}{r_{sat}^2}\int_{\phi=0}^{\frac{179.98}{180}\pi}\int_{\theta=0}^{\frac{179.98}{180}\pi}\int_r^R r^2\sin(\theta)drd\theta d\phi\Big[\approx \frac{2\pi\rho G}{3r_{sat}^2}(R^3 - r^3)\Big] = 1.10297\text{ms}^{-2} \tag{35}$$

where the centre of mass of a hollow hemisphere is approximately halfway between the upper and outer radius, therefore $r_{sat} = 3571 + 1400 + 225 = 5196$ km.

Performing gravity calculations on a spherical chunk allows for a significant increase in radial resolution whilst avoiding lateral oversampling. However, edge effects due to the absence of mass adjacent to the model corrupts a significant portion of the measured gravity field. The trade-off between an increase a radial resolution versus the influence of edge effects is investigated through the uniform spherical chunk benchmark which is performed with a model of GMR=8 featuring an increase in quadrature points to 64 points (total model resolution being resolution of $0.7^\circ \times 0.7^\circ \times 1.3$km):

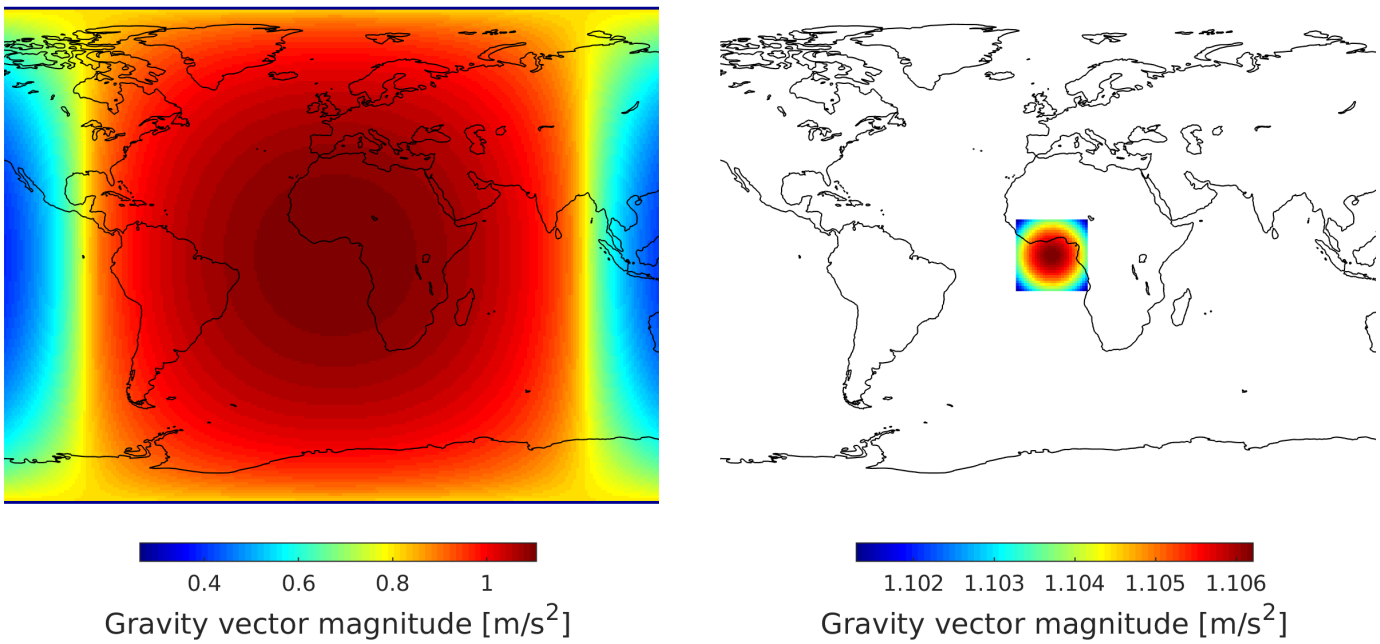

Figure 7: *a) The gravitational signal, including edge effects, for a spherical hemisphere. b) The surface area of the spherical chunk that contains less than* 0.1% *deviation from the analytical signal.*

The gravity computed on a uniform spherical chunk yields a maximum vertical gravity vector of $\vec{g} = 1.1062\text{ms}^{-2}$, which deviates 323 mgal from the analytical value of 1.10297ms^{-2}. This discrepancy is due to, firstly, ASPECT's integration kernel not being a polynomial yet also because of the discrepancy between the domain boundaries in the analytical solution and the model ($[-89.99^\circ : 89.99^\circ]$ versus $[-90^\circ : 90^\circ]$), and the subsequent misplacement of the centre of mass. Shown

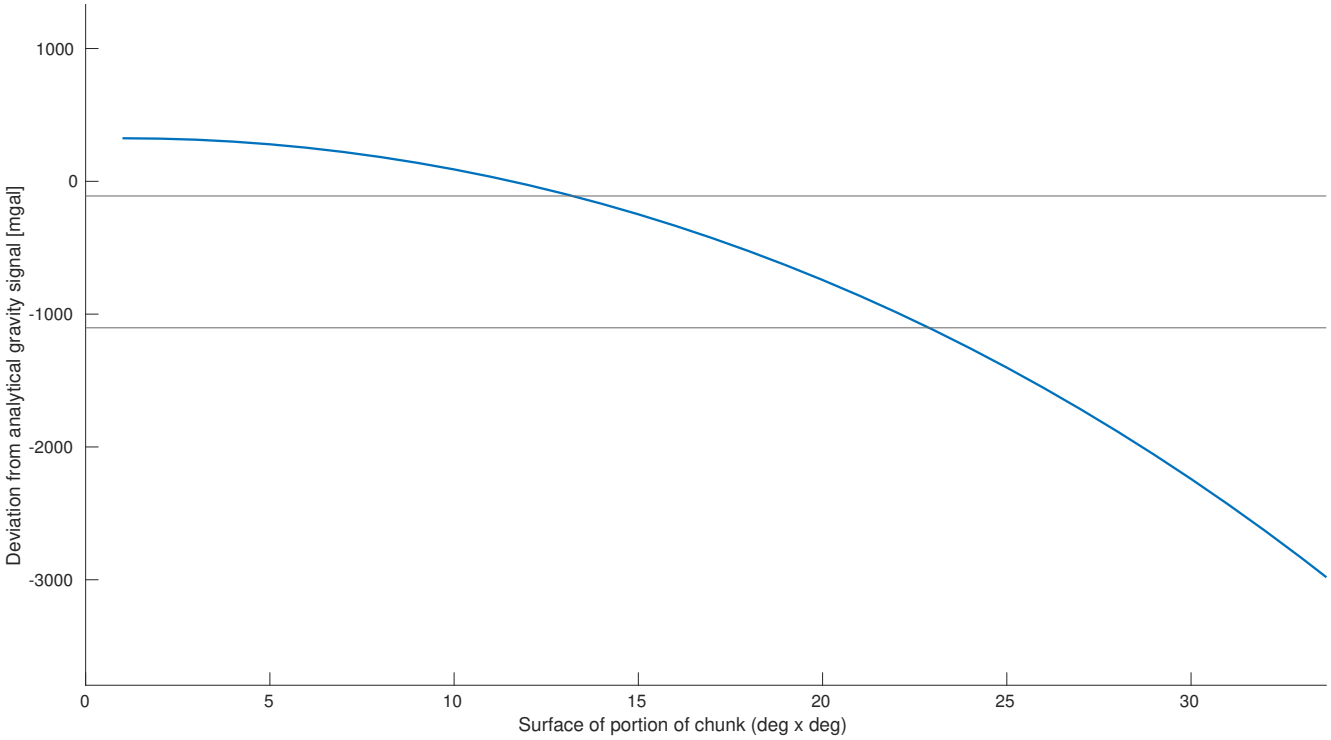

Figure 8: *The deviation between the analytical magnitude and the maximum error per scrutinized surface area of the spherical chunk. The horizontal lines represent* 0.1% *and* 1% *of the analytical gravity magnitude.*

in figure 7, the gravitational signal rapidly deteriorates towards the edges. The deviation between the analytical gravity magnitude and computed gravity magnitude per scrutinized portion of the spherical chunk is plotted in figure 8. The 2 horizontal lines represent a error margin of 0.1% and 1% with respect to the analytical value; which yield maximum surface areas of $13^{\circ} \times 13^{\circ}$ (Figure 8) and $22^{\circ} \times 22^{\circ}$, respectively. To conclude, using a spherical chunk geometry and allowing for a 0.1% error means that a meager $\sim 2.1\%$ of the model contains reliable data.

3.1.3 Synthetic LLSVP

In the pursuit of a mantle density model, the discussion revolves around the scaling of seismic wave perturbations. Large Low Shear Velocity Provinces (LLSVPs) (Dziewonski et al. (1977)) are the largest-scale seismic anomalies in the Earth's mantle and these, too, are up for debate. The sources of the two LLSVPs (African and Pacific) are simultaneously explained as lighter-than-average material (Koelemeijer et al. (2017)) and denser-than-average material (Garnero and McNamara (2008); Ishii and Tromp (1999)). Thermal variations would allow lower mantle material to become lighter, whereas chemical heterogeneity (e.g. the presence of post-perovskite or slab remnants) would cause lower mantle material to become denser. Roughly, all proposed models of estimated density perturbations fall in the range of $-1\% \leq \delta \ln \rho \leq 1\%$. From the visualization of tomographic data set SP12RTS (Koelemeijer et al. (2015)) a back-of-the-envelope estimate of the spatial dimensions of these anomalies was established (figure 9).

This final benchmark consists of a uniform global mantle with a density anomaly, located on the CMB, of $60^\circ \times 70^\circ \times 700$km, which is the approximate size of the African LLSVP (see figure 10). Two end-member tests are performed: a denser-than-average scenario and a lighter-than-average scenario. From this benchmark, the gravity signals of both end-member LLSVP's can be inferred. Moreover, the spectral range in which these anomalies are visible can be deducted by decomposing the scalar field into spherical harmonics and re-synthesizing in the desirable spectral range.

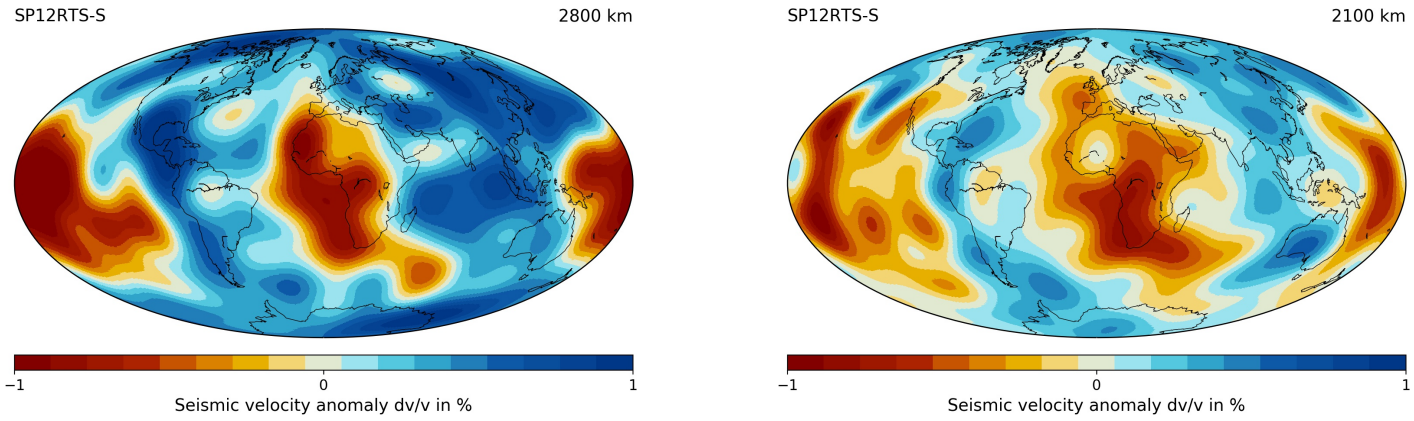

Figure 9: *A visualization of tomographic model SP12RTS (Koelemeijer et al. (2015)) for depth slices at a) 2800 km depth, and b) 2100 km depth. The lower-than-average wave speeds apparent underneath Africa embody the LLSVP. The spatial dimensions are deduced from this model; the depth slice at 2100 km depth is the last depth slice to show a single distinct anomaly and is taken as the top of the LLSVP.*

The gravity anomaly fields computed by ASPECT (GMR=8 and 8 quadrature points) for the synthetic LLSVP benchmark tests both yield a deviation of ± 47 mgal for the complete spectrum. Whilst having the mean (d/o 0) removed with the spherical harmonics software, the signal remains comparable although the amplitude of the anomaly deteriorates from ± 47 mgal to ± 30 mgal. This can be attributed to the spherical harmonics approximation of the tesseroidal geometry used in ASPECT being imperfect for a $1^\circ \times 1^\circ$ resolution (Root et al. (2016)), in combination with the steep LLSVP-boundaries used for this benchmark. The gravity anomaly fields, for both the denser-than-average and lighter-than-average LLSVP's, are spectrally filtered over multiple large wavelength spectra. The gravitational fields for the two different scenario are anti-correlated, yielding identical anomaly magnitudes.

Figures 11 and 12 show the gravity anomaly fields for the synthetic LLSVP's over specific spectra. The gravitational

signals of these lower mantle anomalies exist exclusively in the spectral range d/o 1-4 (>5000 km), of which the bulk of the amplitude resides in d/o 1-3. In the spectral range d/o 5-179 the shape of the anomalies can no longer be deducted and the gravity anomaly magnitude is less than 2% of the total signal. In compliance with Sebera et al. (2018) and Hager et al. (1985), density perturbations of no larger than ±1% originating in the lower mantle reside mostly in the range d/o 1-3 (> 6600 km).

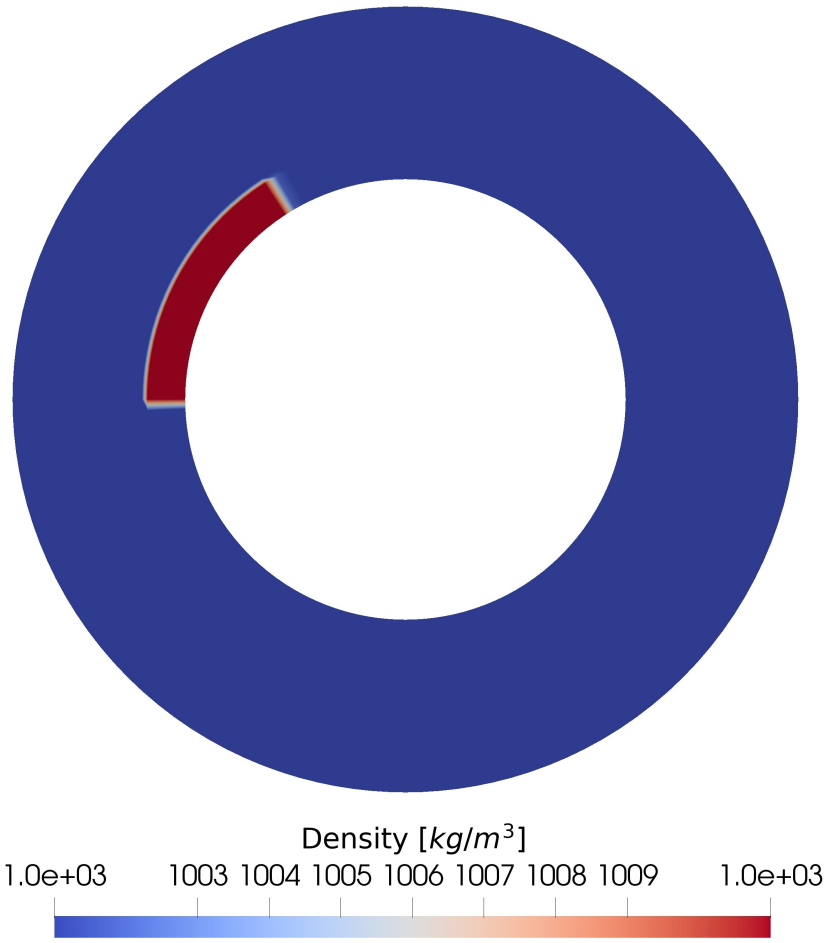

Figure 10: The model in ASPECT including a denser-than-average LLSVP.

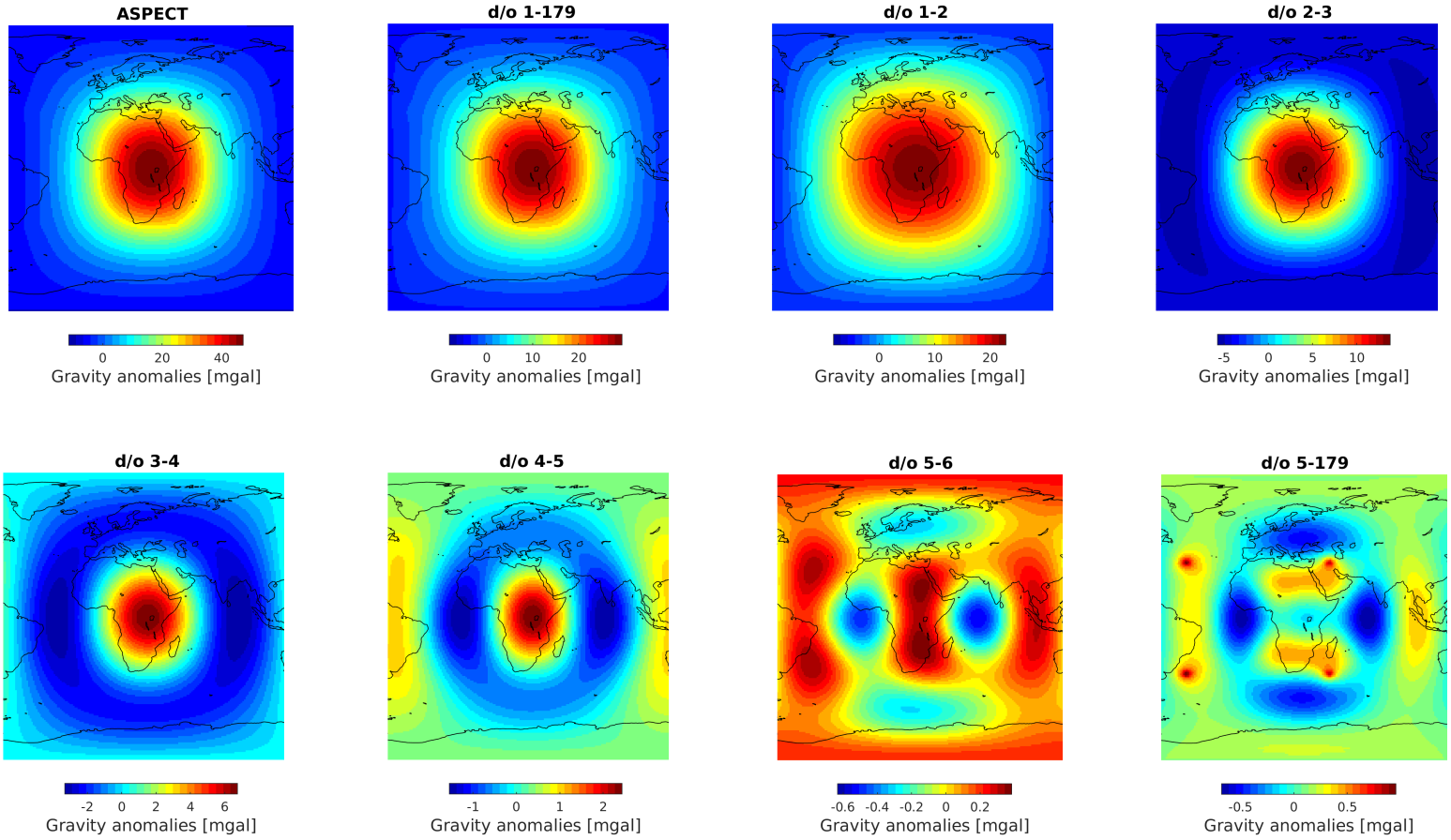

Figure 11: *The denser-than-average synthetic LLSVP computed in a) ASPECT and b-h) the decomposed, filtered and subsequently re-synthesized anomaly fields in specific spectral ranges.*

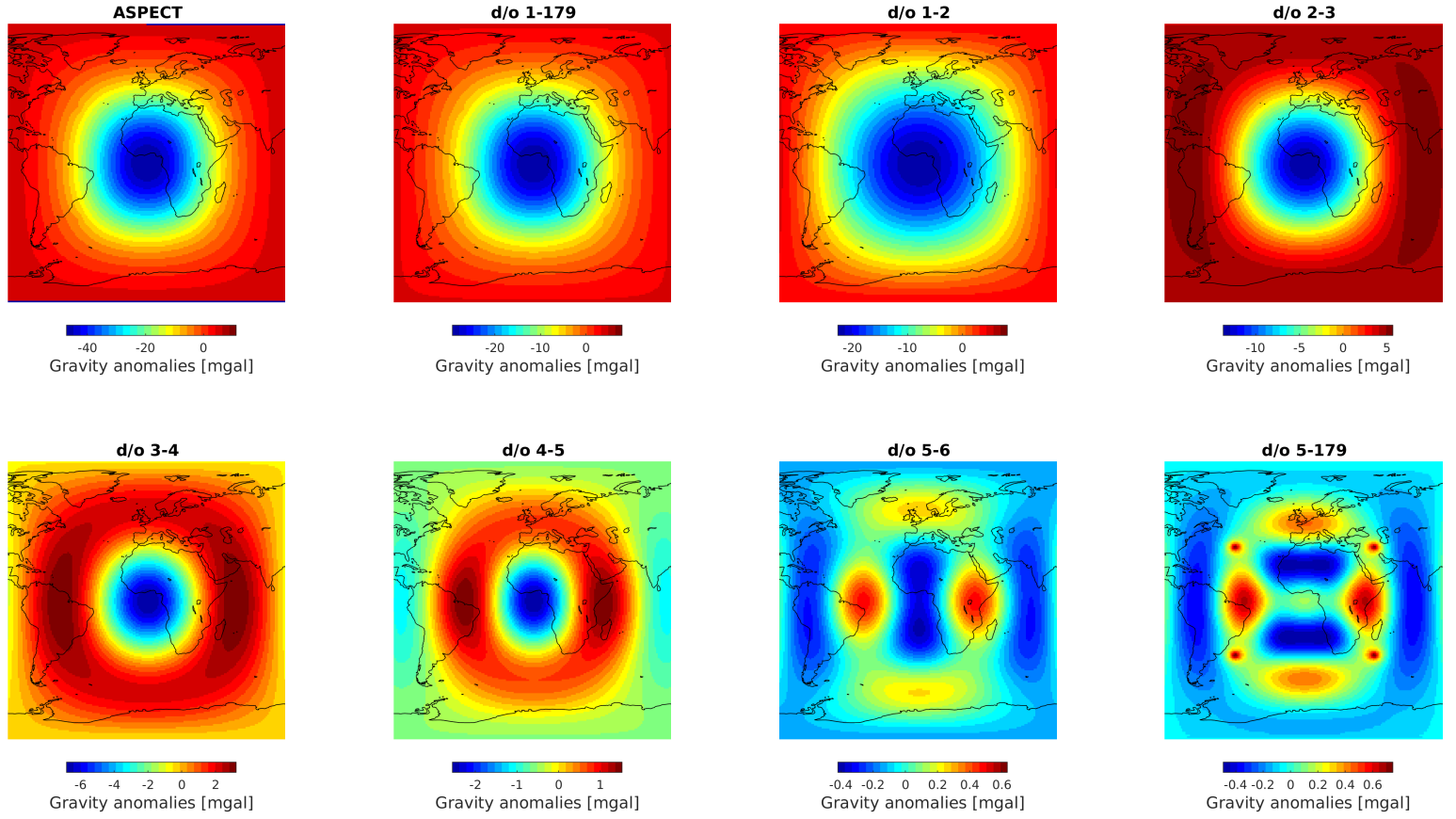

Figure 12: *The lighter-than-average synthetic LLSVP computed in a) ASPECT and b-h) the decomposed, filtered and subsequently re-synthesized anomaly fields in specific spectral ranges.*

3.2 CRUST1.0

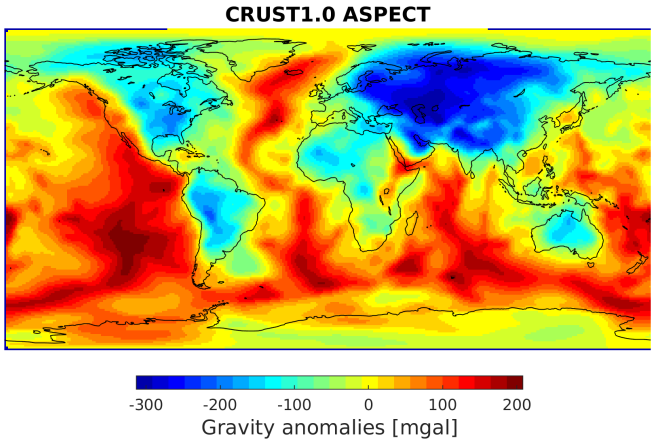

Figure 13: *The gravity anomaly scalar field for CRUST1.0, computed through ASPECT.*

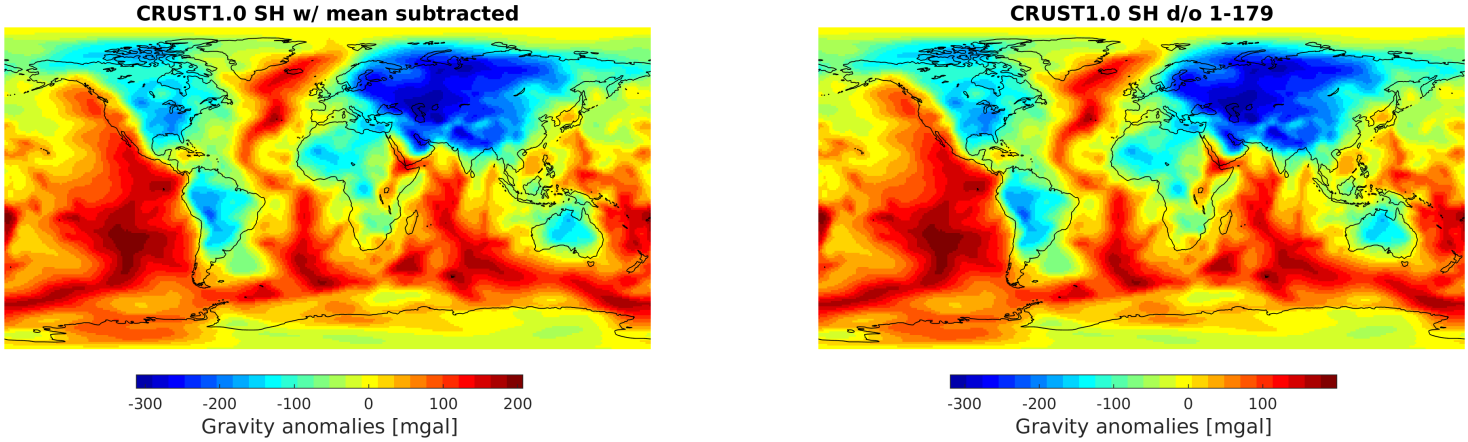

Figure 14: *a) The gravity anomaly as computed using the spherical harmonics approximation, subtracting the mean of the field. b) The gravity anomaly as computed using the spherical harmonics approximation, omitting the first spherical harmonic (d/o 1-179).*

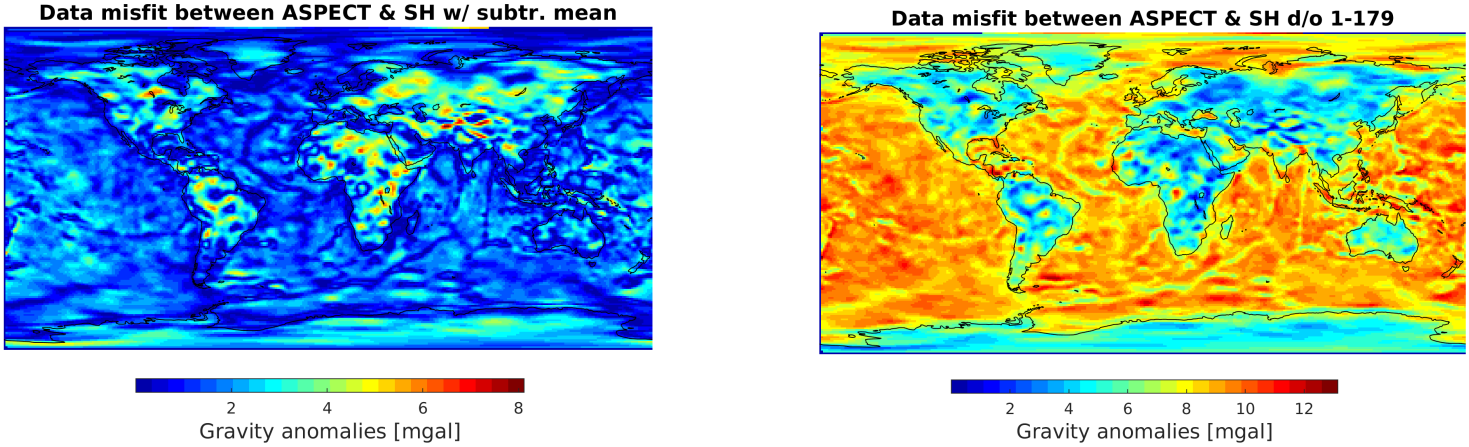

Figure 15: *a) The absolute value of the difference between the gravity anomaly field of CRUST1.0 from ASPECT and from the spherical harmonics approximation, having subtracted the mean of the field. b) The absolute value of the difference between the gravity anomaly field of CRUST1.0 from ASPECT and from the spherical harmonics approximation, having subtracted the first spherical harmonic (d/o 1-179).*

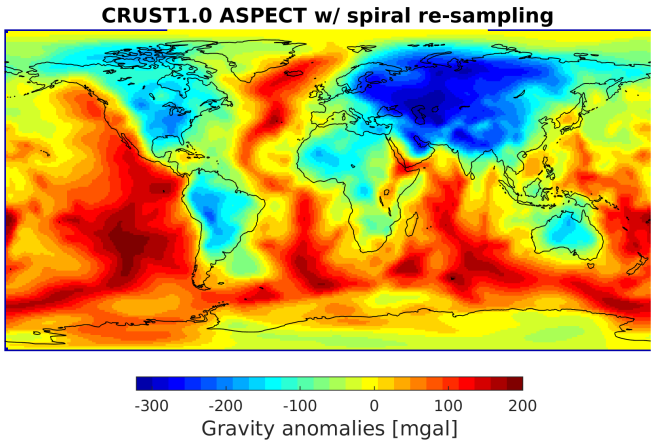

Figure 16: *The gravity anomaly scalar field for CRUST1.0, computed through ASPECT and subsequently re-sampled.*

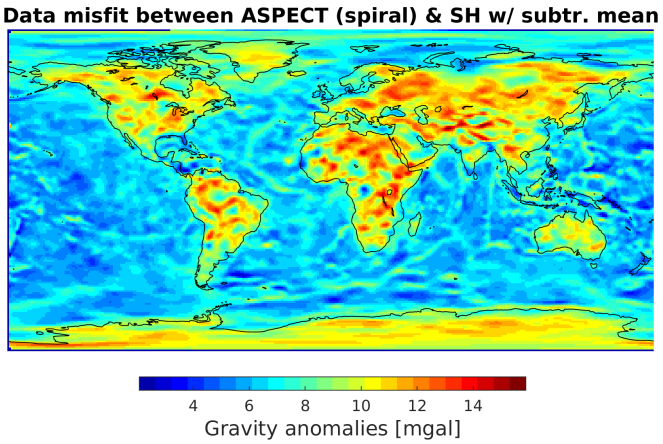

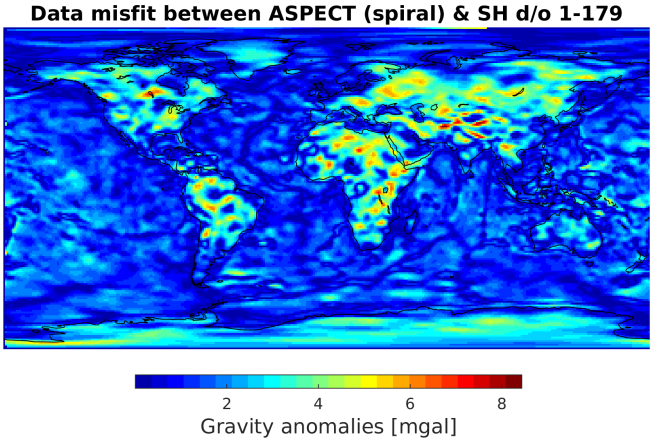

Figure 17: *a) The absolute value of the difference between the gravity anomaly field of CRUST1.0 from ASPECT (after re-sampling) and from the spherical harmonics approximation, having subtracted the mean of the field. b) The absolute value of the difference between the gravity anomaly field of CRUST1.0 from ASPECT (after re-sampling) and from the spherical harmonics approximation, having subtracted the first spherical harmonic (d/o 1-179).*

In this section, the gravitational signal of the CRUST1.0 data set is computed using both the direct integration (ASPECT) and the spherical harmonics method. This data set contains a density distribution from the free surface to the Moho discontinuity, under which it is filled with a constant density of 3300kgm^{-3} until a depth of 80 km. The data of model CRUST1.0 are not formatted in a equidistant 3D mesh, like the tomography models. The lateral resolution of the crustal model is $\sim 1^{\circ} \times 1^{\circ}$, however, radially it is composed of distinct layers whose interfaces yield a radial resolution of 10m. Due to computational limitations, the data is projected on an equiangular mesh with a radial resolution of 100m. When increasing the resolution of the model in ASPECT, the gravity field of CRUST1.0 converges to a stable gravity field. The models in ASPECT were computed using GMR=8 and 64 quadrature points per mesh cell.

The highest compatibility between the models from the direct integration method and the spherical harmonics approximation method yields a maximum error of 8.44 mgal (figures 15a and 17b). Two techniques achieved the same data misfit. The best fit between the two gravity field were, firstly, subtracting the mean from the ASPECT (figure 13) and spherical harmonics gravity field (figure 14a) without re-sampling the gravity field from ASPECT. Secondly, identical results were achieved by spectrally removing the mean in the spherical harmonics gravity field (d/o 1-179) (figure 14b) and re-sampling the gravity field from ASPECT (figure 16). The discrepancies between the models mostly reside in continental data, however, seems to be largely uncorrelated to (Moho) topography.

The gravity signal of CRUST1.0 shows low gravity signal for the majority of continental crust, especially the Eurasian continental crust. Mid-ocean ridges consistently show positive anomalies as well as, albeit to a lesser degree, subduction zones.

3.3 Tomographic models

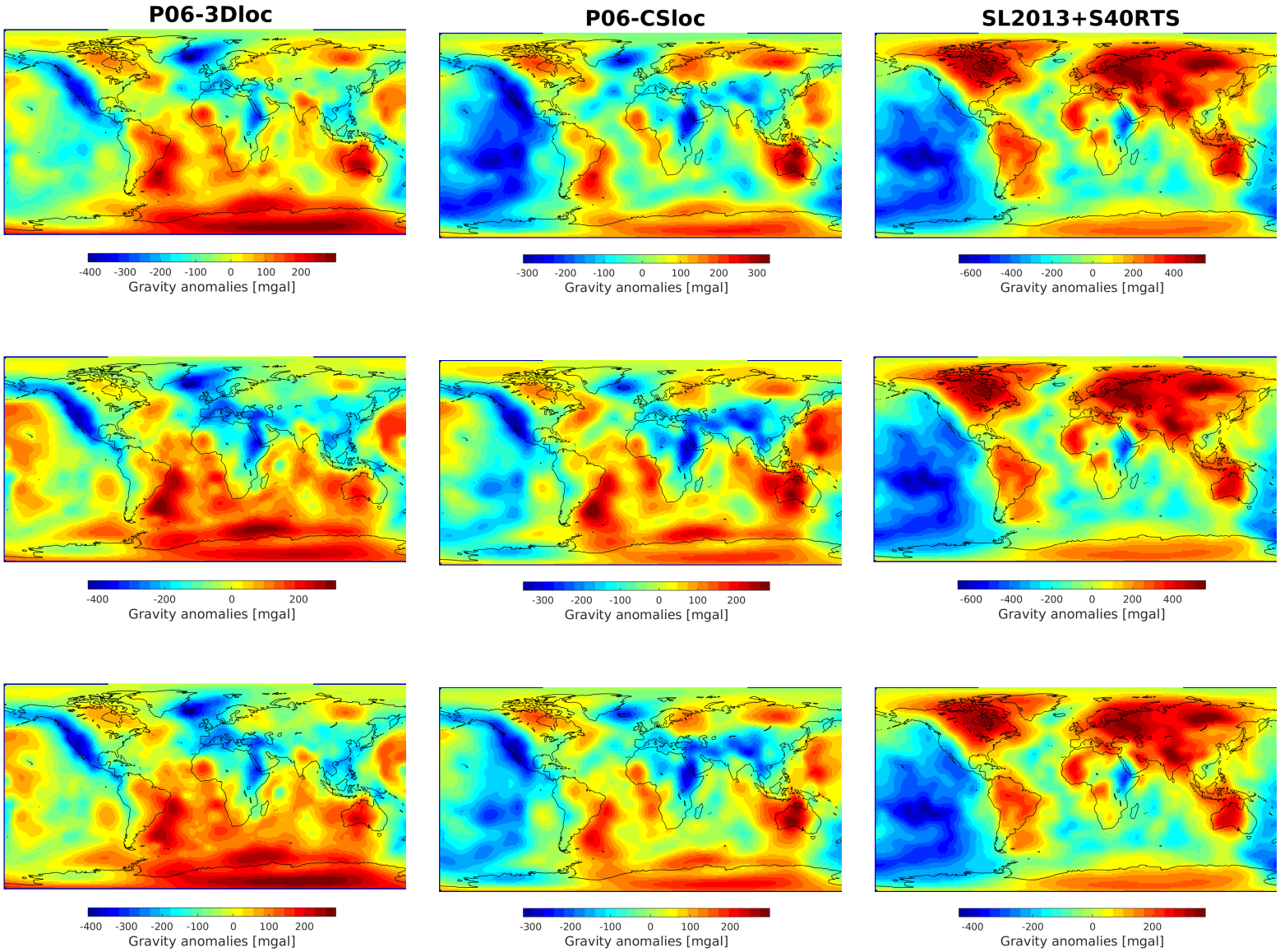

Figure 18: *The left column is the gravity field for tomographic data set P06-3Dloc (Amaru (2007)), for resolution of GMR=6 (top), GMR=7 (middle) and, the highest resolution achievable, GMR=8 with 64 quadrature points (bottom). The middle column is the gravity field for tomographic data set P06-CSloc (Amaru (2007)), for resolution of GMR=6 (top), GMR=7 (middle) and GMR=8 with 64 quadrature points (bottom). The right column is the gravity field for tomographic data set SL2013+S40RTS (Amaru (2007)), for resolution of GMR=6 (top), GMR=7 (middle) and GMR=8 with 64 quadrature points (bottom).*

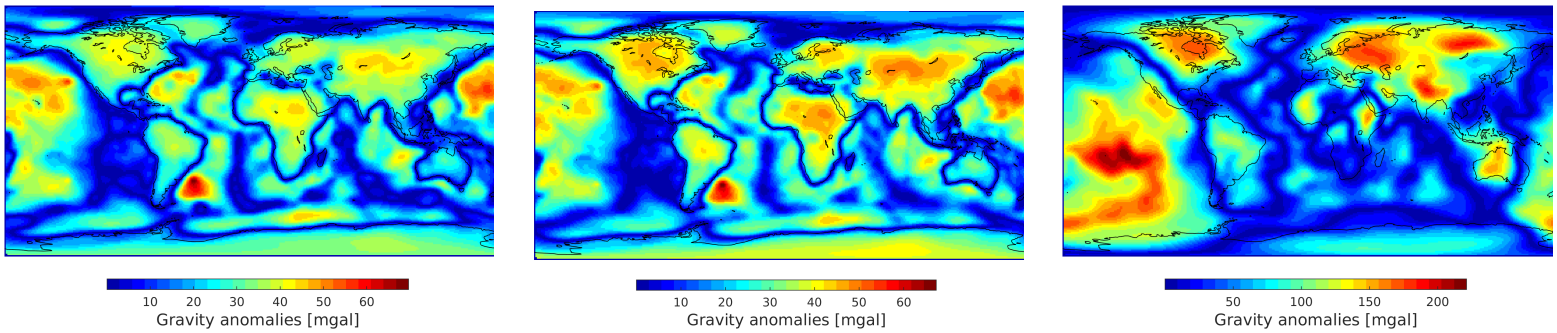

Figure 19: *The absolute misfit between the tomographic models computed for resolution GMR=7 and the highest achievable GMR=8 with 64 quadrature points. Again, the left data set is P06-3Dloc, the middle is P06-CSloc and the right is SL2013+S40RTS.*

Figure 18 shows the gravity fields of the three utilized data sets with increasing resolution from top to bottom. These data sets are tomographic data sets from Amaru (2007) and consist of wave speed perturbations ($\partial v_s/v_s(z)$ for the SL2013+S40RTS data set and $\partial v_p/v_p(z)$ for the P06-CSloc and the P06-3Dloc data sets). Here, the tomographic models have been scaled using constants which do not depend on the depth of the model. These constant are:

$$\frac{\partial \ln \rho}{\partial \ln V_s} = 0.25 \quad \text{and} \quad \frac{\partial \ln V_s}{\partial \ln V_p} = 1.5 \tag{36}$$

after Ghosh et al. (2017) and in the proposed range of Karato (1993); Resovsky and Trampert (2003).

The lowest of three panels of figure 18 show the computationally highest achievable resolution, being 201,326,592 mesh cells and a vertical resolution of 10.94 km, whereas the vertical resolution of the data is 10 km. All three tomographic do not converge towards a stable gravity field; therefore a potential error is introduced by vertically undersampling. Although this error remains unknown, the absolute misfit between the gravity fields calculated before and after the final global mesh refinement step is shown in figure 19. The maximum discrepancies yield 67.35 mgal for data set P06-CSloc, 69.68 mgal for data set P06-3Dloc and 221.25 mgal for data set SL2013+S40RTS. Although the error between the highest achievable gravity fields and the true models will likely be less, since the vertical model resolution is in the vicinity of the vertical data resolution, this at least offers a grasp on the order of magnitude.

The gravity signal of the tomographic data sets consistently shows a negative anomaly for the East-African rift. In addition, the models P06-CSloc and P06-3Dloc clearly resolve the majority of prominent subduction zones (North- and South American subduction zone, the Pacific subduction zones as well as the Tethys suture zone) in the form of negative anomalies. All models mutually disagree on the gravity signal underneath oceans and prominent cratons. From figure 19 we can deduct that further improving the vertical resolution of the model will improve the gravity signal of cratons and oceans. In particular, in models P06-CSloc and P06-3Dloc, the gravity signal of the Falkland plateau would benefit from increased resolution. In model SL2013+S40RTS this is the case for the gravity signal of the Pacific Ocean.

3.4 Scaling sensitivity

In this section, the sensitivity of the gravitational signal of the tomographic data sets as presented in section 3.3 to depth-dependent scaling factors is computed. This research uses scaling factors from Steinberger and Calderwood (2006) and Moulik and Ekström (2016). The scaling from Steinberger and Calderwood (2006) comprises the $\partial \ln\rho / \partial \ln V_s$-scaling only, therefore the P06-3Dloc and P06-CSloc data sets are scaled from compressional wavespeed to shear wave speed with the constant from section 3.3. In contrast, the scaling from Moulik and Ekström (2016) contain both the $\partial \ln\rho / \partial \ln V_s$ as well as the $\partial \ln V_s / \partial \ln V_p$. However, the scaling from Steinberger and Calderwood (2006) contains a data at a 10 km vertical resolution (2891 data points), whereas the scaling from Moulik and Ekström (2016) contains 23 data points only for the entire mantle. The scaling relations from Moulik and Ekström (2016) show much larger amplitudes as opposed to the more conservative scaling from Steinberger and Calderwood (2006). The scaling relations are plotted in figures 20.

Moulik and Ekström (2016) used surface wave phase anomalies, body wave travel times, normal-mode splitting functions and long-period waveforms to construct a joint model in order to detect signatures of chemical heterogeneity throughout the mantle. Noticeably, their model yields an denser-than-average anomalies in the lowermost mantle, as opposed to the scaling by Steinberger and Calderwood (2006) whom construct their depth-dependent scaling not from seismological constraints but from thermal contributions to seismic wave speeds perturbations in combination with a depth-dependent model of thermal expansivity, as established by Karato (1993).

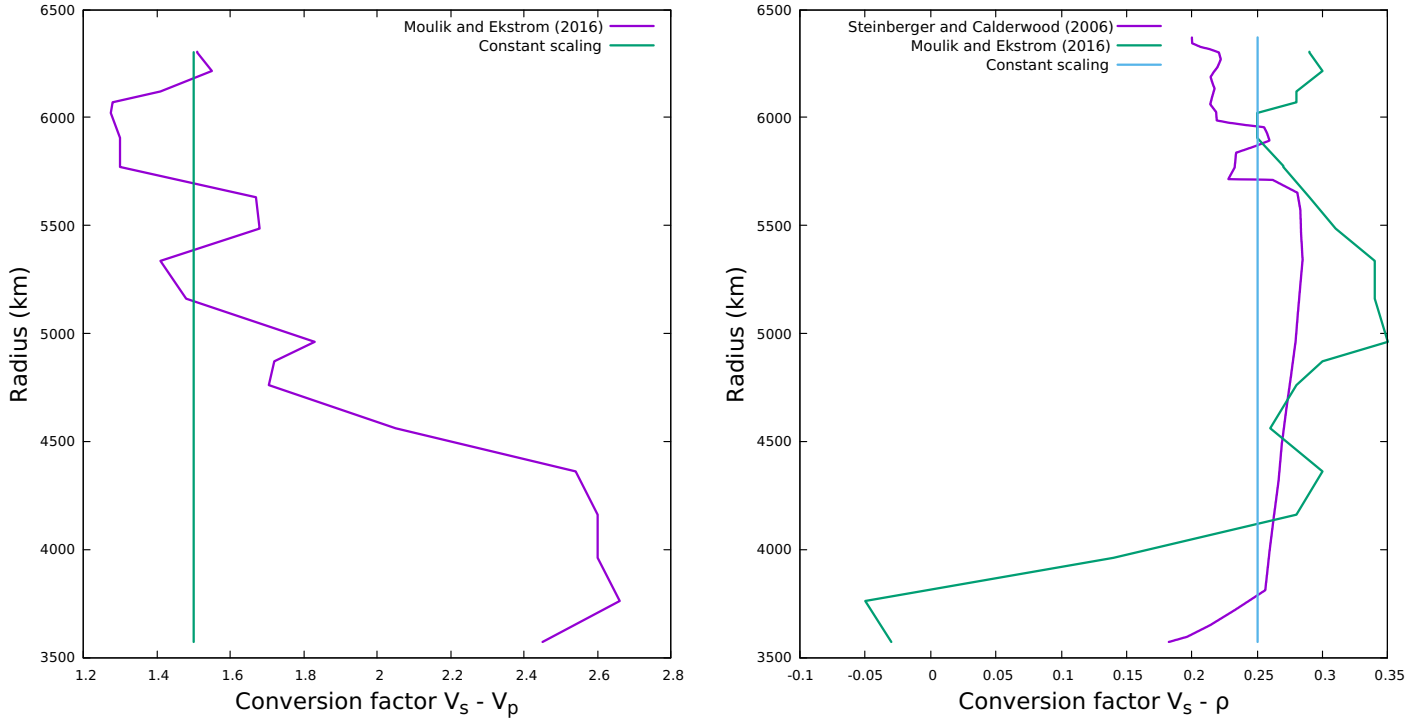

Figure 20: *The scaling relations between V_s and V_p (left) and between V_s and ρ.*

3.4.1 Steinberger and Calderwood (2006) scaling

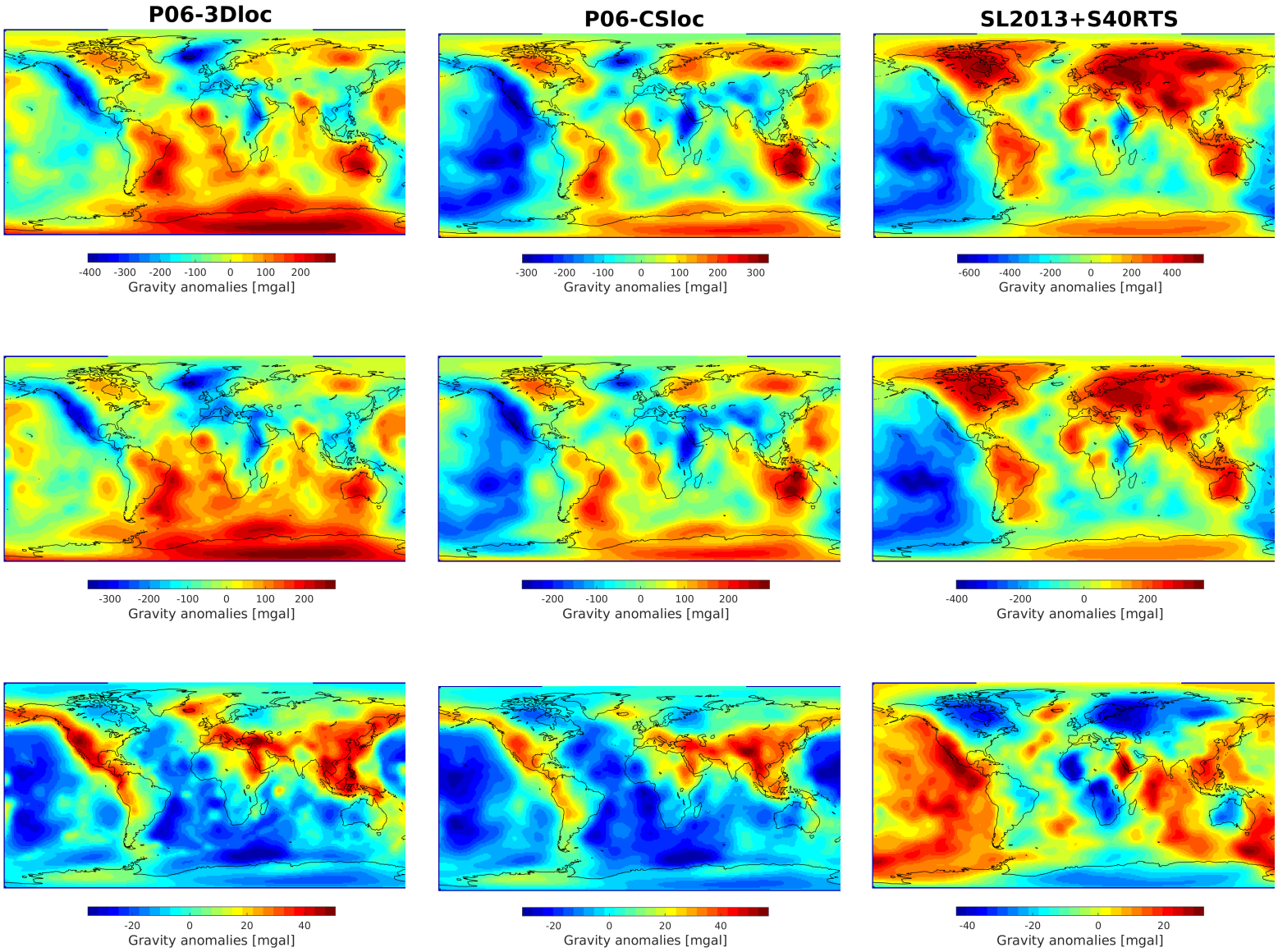

Figure 21: *The left column is the gravity field for tomographic data set P06-3Dloc (Amaru (2007)), with a constant scaling (top), with the Steinberger and Calderwood (2006) scaling (middle) and the misfit between the two (lower). The middle column shows the same for P06-CSloc and the right column for SL2013+S40RTS.*

Utilizing a depth-dependent conversion between shear wave speeds and density, as opposed to a constant value, leads to substantially different gravity anomaly magnitudes. The P06-3Dloc model (left panels in figure 21) show significantly weaker negative anomalies at nearly all converging plate boundaries (Thethys suture, both North- and South American subduction zones, the Pacific and the Japan-Izu-Bonin subduction zones). Oceanic regions structurally obtain a higher gravitational signal when scaled according to Steinberger and Calderwood (2006). The largest discrepancy between the constant scaling and the depth-dependent scaling for this data set is 50.83 mgal, located at converging plate boundaries.

The depth-dependent scaling has a similar effect on data set P06-CSloc (middle panels in figure 21) in the form of a weaker gravitational signal for convergent plate boundaries and a higher gravitational signal for oceanic regions, however, the amplitude of the misfit is consistently lower with respect to P06-3Dloc. The largest discrepancy between the anomaly fields from the constant scaling and the depth dependent scaling is 57.17 and originates in the Himalayan plateau.

The tomographic model SL2013+S40RTS is least affected by the depth-dependent scaling. Contrary to the models of compressional wave speeds, the scaling here decreases the gravitational signal of oceanic regions and increases the gravitational signal of prominent cratons (e.g. West-Australia, West Africa, North-Africa and Siberia). There lay the the largest discrepancies between the anomaly fields from the constant scaling and the depth dependent scaling, with a maximum of 43.43 mgal.

3.4.2 Moulik and Ekström (2016) scaling

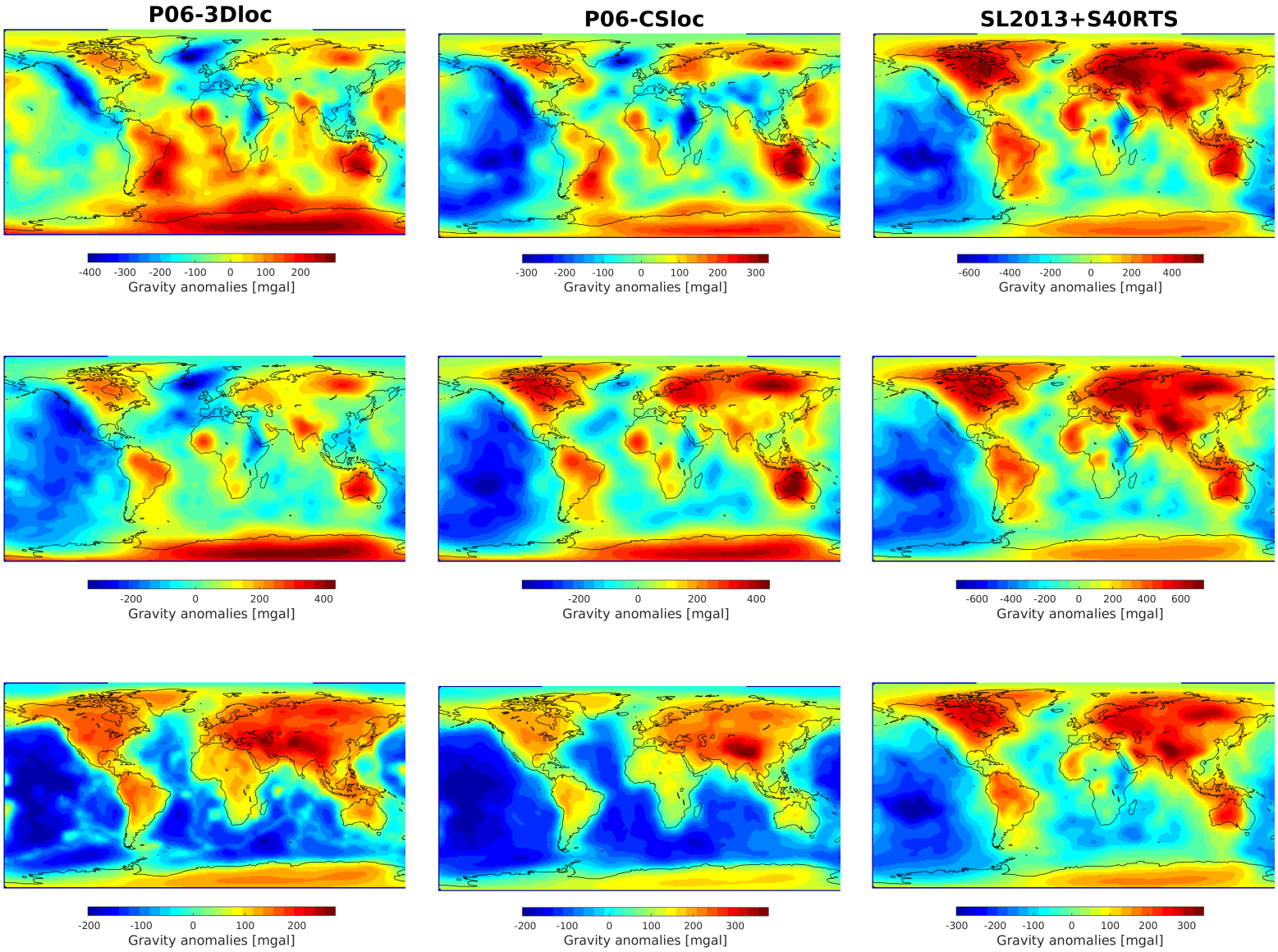

Figure 22: *The left column is the gravity field for tomographic data set P06-3Dloc (Amaru (2007)), with a constant scaling (top), with the Moulik and Ekström (2016) scaling (middle) and the misfit between the two (lower). The middle column shows the same for P06-CSloc and the right column for SL2013+S40RTS.*

The second depth-dependent conversion (Moulik and Ekström (2016)) contains both a scaling from compressional wave speeds to shear wave speeds and, subsequently, the scaling from shear wave speeds to density; the results shown are an expression of a convolution between the two. The largest differences between this conversion and the one proposed by Steinberger and Calderwood (2006) are the significantly larger amplitudes and the anti-correlation between the shear wave speeds and density in the lowermost mantle.

The P06-3Dloc and P06-CSloc models (left and middle panels in figure 22, resp.) show significantly stronger positive anomalies for all continental regions, and vice-versa a significantly stronger negative anomaly for all oceanic regions. This is to be expected since the conversion factors is larger for shallower zones, which contribute the most to the gravitational signal since gravity deteriorates quadratically with distance. The largest discrepancy between the anomaly fields from the constant scaling and the depth dependent scaling is 274.29 mgal for P06-3Dloc and 379.48 mgal for P06-CSloc; the peaks originate in the Himalayan plateau. The SL2013+S40RTS model (right panels in figure 22) shows consistent behaviour with respect to P06-3Dloc and P06-CSloc; the only difference being the decreased gravitational signal for the East-African Rift region. The largest discrepancy between the anomaly fields from the constant scaling and the depth dependent scaling is 345.42 mgal for the SL2013+S40RTS.

3.5 Composite models

The data sets from sections 3.2 and 3.3 (crustal and tomographic, resp.) are merged in an effort to simulate the Earth's gravitational field. As a result of the difference in data resolution, CRUST1.0 having a vertical resolution of 10 m and the tomographic models having a resolution of 10 km, merging this data serves, computationally speaking, as a challenge due to the model's memory complexity. The largest achievable composite data set keep their original tomographic resolution yet contain a crustal vertical resolution of 500 m, as opposed to the gravitational fields from section 3.3 which contains a 100 m vertical resolution. Decreasing the resolution of CRUST1.0 in order to reduce the size of the data set introduces an error in the computation of the density field, this is quantified in section 4.

As a result of computational limitations, building the mesh for combined data sets also presents a trade-off between crustal resolution and mantle resolution. Utilizing the mesh-building feature 'Minimum Refinement Technique' (see section 2) allows for extra refinement for specifiable radii, making it possible to refine crustal regions without oversampling the mantle. Finally, the data set is computed with a starting mesh of 25 million cells (GMR=7) after which 3 additional levels of refinement will be applied for data with a radius between 6291 and 6377 kilometers, marking the top and bottom of the CRUST1.0 data set. This yields a mesh comprising of ∼434 million cells and a vertical resolution of 21.9 km for the tomographic data and 2.7 km for crustal data, therefore all data is undersampled and consequentially this reduces accuracy of the results. For the tomographic data, the error introduced here is not quantifiable because these models failed to converge before merging. The difference between the gravity produced by these data sets for GMR=7 and GMR=8 is shown in figure 19 and yields a minimum error of 69.68 mgal for P06-3Dloc, 67.35 mgal for P06-CSloc and 221.5 mgal for SL2013+S40RTS.

Global GMR	Crustal increase GMR	Nr. of cells	Vert. mantle resolution	Vert. crust resolution
7	0	25,165,824	21.93 km	21.93 km
7	1	30,670,848	21.93 km	10.75 km
7	2	76,087,296	21.93 km	5.38 km
7	3	433,913,856	21.93 km	2.67 km

Table 3: *The mesh for GMR=7 and the subsequent crustal refinement, and the vertical resolution both data sets.*

The process of merging the data is not trivial. CRUST1.0 is made up of compositional layers with depth variable interfaces; the bottom one being the Moho. The original CRUST1.0 data set has 'filled' everything beneath the Moho until a depth of 80 km with a constant density of 3300 kgm^{-3}. Conveniently, all data above the Moho does not exceed 3050 kgm^{-3}. When merging the data sets, the lateral heterogeneity of CRUST1.0 does not allow for 'pasting' the data atop one another at a specific depth. Instead, CRUST1.0 was kept intact for $\rho < 3300\text{kgm}^{-3}$ only, or everything above the Moho; the remaining regions of overlap between the data sets were filled with tomographic data projected on the mesh and, closer to the Moho interface, an interpolation of tomographic and crustal data.

This method is not flawless; in oceanic regions, the radial density profile shows a significant density decrease with depth which is physically unlikely. Figure 23 shows a radial for a continental point (purple) and for an oceanic point (green). The continental density profile solely increases with depth and looks, considering these are discrete points, relatively smooth. The radial density profile from the oceanic region shows several large density jumps; the first large density decrease being the interface between the two data sets, the deeper density jumps originate in the tomographic data. This density jump caused by merging the data will have an unsound effect on the gravitational signal. Moreover, taking into account the high amplitude perturbations of the tomographic data sets in the shallow zones (wave speeds perturbations exceeding 25%), this additional density jump merely adds to the unrealistic nature of the shallow part of the density profile.

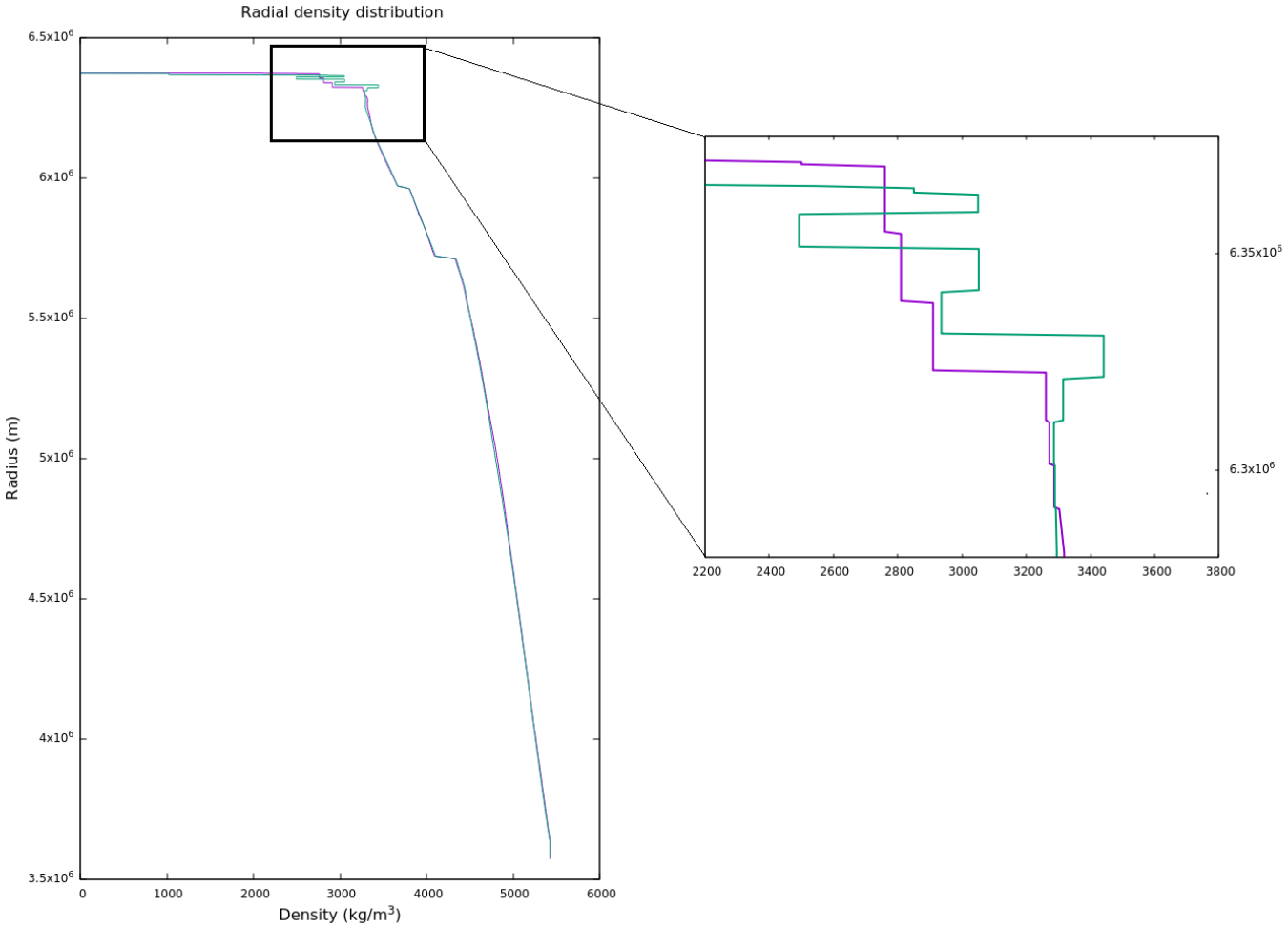

Figure 23: *The radial density distribution for two points in the model, the purple line represents a density profile sampled in a continental region and the green line represents a density profile sampled in an oceanic region. The zoomed-in image shows density jumps near the Moho for the oceanic region.*

Figure 24 shows the gravitational signal for the composite data sets with all three scaling profiles. All three models show significantly higher anomaly amplitudes when scaled according to Moulik and Ekström (2016). Moreover, all models consistently show strong positive anomalies in continental regions and strong negative anomalies for oceanic regions. The P-wave models show strong positive anomalies for especially cratons, the S-wave model for all continental areas with the exception of the East-African Rift.

The clear exaggeration of the continental gravitational signal may have its origin in (the lack of) lithospheric data. Aforementioned, all tomographic data sets yield extremely high wave speed perturbations, often exceeding 25-30%, in the upper 50 km. In combination with the 1D reference density profile ak135 (Kennett et al. (1995)), which yields values of $2450-2710\text{kgm}^{-3}$ in the upper 35 km, this leads to an underestimation of density in the upper mantle material, specifically in oceanic regions, hence the strong negative oceanic anomalies. This issue can be avoided by either including data containing the lithosphere and the lithosphere-asthenosphere boundary (e.g. LITHO1.0 (Pasyanos (2005))), tomographic models with greater resolution in the lithosphere, or employ a depth-weighted linear average for lithospheric density to circumvent the absence of accurate lithospheric data (see section 4).

The effect of scaling the tomographic data in the composite model has a similar effect as presented in section 3.4, with a slight offset in magnitude of anomaly due to a deviation in the subtracted computed mean of the entire model.

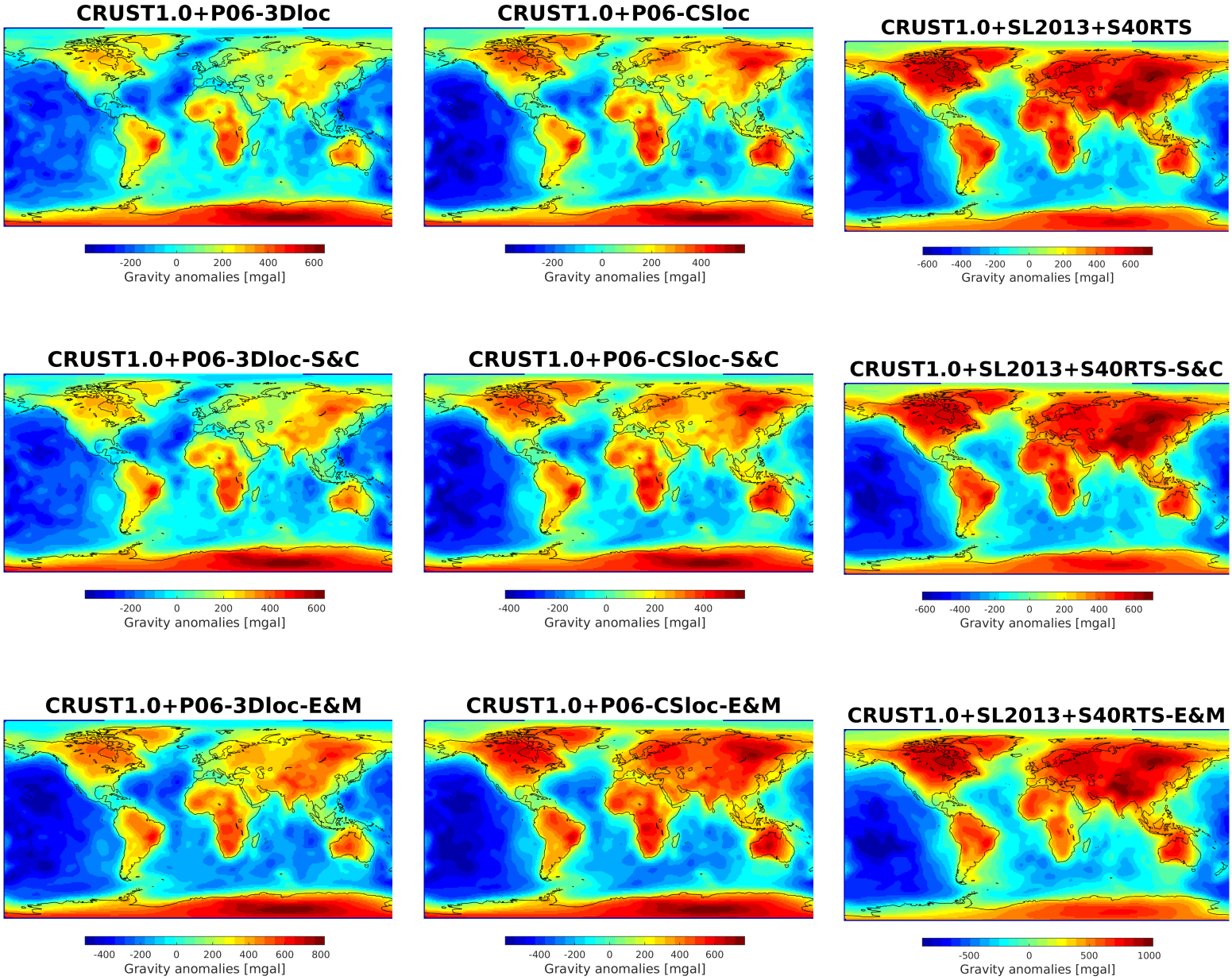

Figure 24: *The left column is the gravity field for the composite data sets P06-3Dloc and CRUST1.0, with a constant scaling (top), with the Steinberger and Calderwood (2006) scaling (middle, denoted as S&C) and the Moulik and Ekström (2016) scaling (lower, denoted as E&M). The middle column shows the same for CRUST1.0+P06-CSloc and the right column for CRUST1.0+SL2013+S40RTS.*

3.6 Spectral analysis

The results of the spectral analysis performed on the composite models from section 3.5 are shown in the appendices 7.2-7.4. The longest wavelength signals of the composite models are scrutinized and visually compared to a similar spectral range of data set GOCO05c. For the synthetic data, the spectral ranges visualized are d/o 1-4 ($\lambda >\sim$ 5000km), d/o 1-6 ($\lambda >\sim$ 3300km), d/o 1-8 ($\lambda >\sim$ 2500km), d/o 1-10 ($\lambda >\sim$ 2000km), d/o 1-30 ($\lambda >\sim$ 650km) and d/o 1-50 ($\lambda >\sim$ 400km). Increasing the spectral range beyond this point does not alter the gravitational field significantly. Simultaneously, the GOCO05c data set is filtered to the same spectral range with the exception of the first spherical harmonics available being 3 as opposed to 1. In the satellite data, the first 3 spherical harmonics coefficients (d/o 0-2) represent the reference oblate spheroid; when subtracted the anomaly field remains.

The longest wavelength anomalies in the GOCO05c satellite data (appendices 7.2-7.4) shows positive anomalies in regions coinciding with subduction around Indonesia and South America, the mantle upwelling underneath Iceland and the southern part of the Indian ocean. The longest wavelength gravitational signal (d/o 3-4) does not show any correlation to suspected structure in the deeper mantle; no anomalies can be correlated to LLSVP's. When increasing the spectral range to include shorter wavelength signals, more geological features can be identified (the Tethys suture, Siberian craton, North American craton, Himalayan Plateau etc.).

Firstly, the composite models (both filtered and unfiltered) show notably larger amplitude anomalies as opposed to satellite data. This is, at least partly, due to the omission of the core in the synthetic models, leading to an overestimation of synthetic gravity anomalies. The spectral analysis of the composite models displays a clear polarization between positive continental anomalies and negative oceanic anomalies for d/o ≥ 6. Especially strong positive anomalies reside in cratons and Antarctica. The composite models and the satellite model do not correlate in any spectral range. Moreover, the identification of geological subsurface features, aside from the distinction between continental and oceanic lithosphere, is not possible in any spectral range.

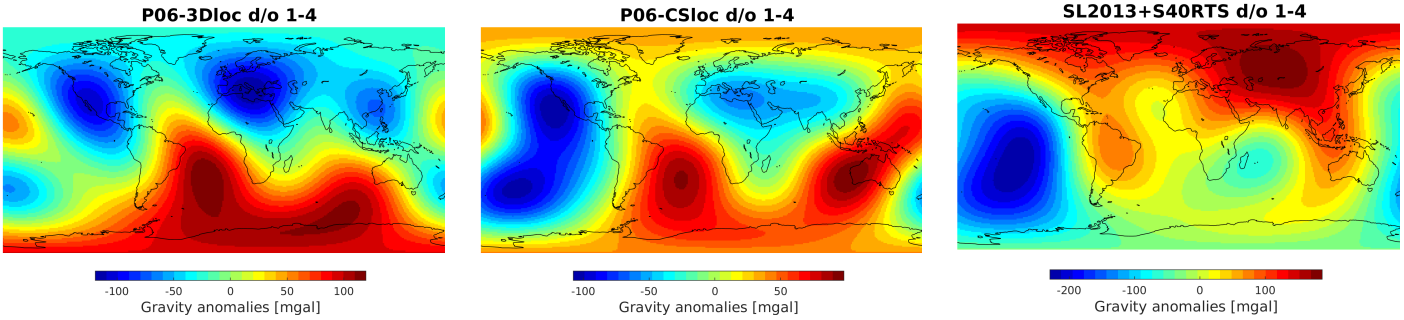

Figure 25: *The longest wavelength gravitational signal (d/o 1-4) of SL2013+S40RTS, P06-3Dloc and P06-CSloc.*

The spectral analysis was also performed on the tomographic models individually (figure 25). The gravitational signal of the individual tomographic models shown below include all data until the surface (without topography). The long wavelength gravitational signal of SL2013+S40RTS shows large positive anomalies over the continents and negative anomalies over the Pacific and African continent. Both P06-3Dloc and P06-CSloc show negative anomalies over South-east Asia, Europe, the Pacific Ocean and North-west America and strong positive anomalies for the Southern Atlantic Ocean and the Southern Indian Ocean and Antarctica, although they differ in anomaly amplitude. All tomographic data sets do not show any correlation to any geological features when filtered to d/o 1-4.

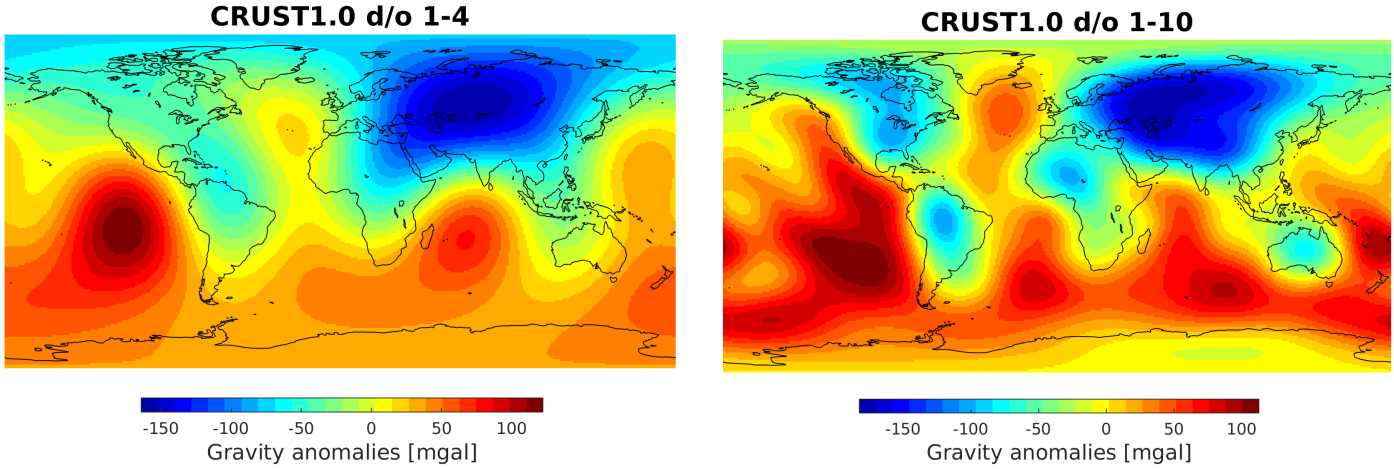

Figure 26: *The longest wavelength gravitational signals (d/o 1-4 and d/o 1-10) of CRUST1.0*

Figure 26 shows the filtered (d/o 1-4 and d/o 1-10) gravity field of the CRUST1.0 model. CRUST1.0 contains data from the surface topography to the Moho. Here, the crustal model is supplemented with material of $\rho = 3300\text{kgm}^{-3}$ until a depth of 80km, identical to the result from section 3.2. The remainder of the CRUST1.0 has a maximum density value of $\rho = 3050\text{kgm}^{-3}$, meaning a density contrast of at least $\Delta\rho = 250\text{kgm}^{-3}$ exists across the Moho. Therefore, the spectral domain (d/o 1-4) of CRUST1.0 might offer some constraints on Moho topography. The gravity field filtered in the range d/o 1-4 shows negative gravity anomalies over the continents (in particular the Eurasian continents) and negative gravity anomalies for most oceanic regions. The gravity field filtered in range d/o 1-10 shows a clearer distinction between continental (especially cratonic) regions and oceanic regions.

4 Discussion

This research is conducted to investigate whether it is feasible to extract information from the Earth's mantle from the gravitational signal of existing data sets. Four data sets were used for gravity calculations: one crustal data set (CRUST1.0) and 3 tomographic data sets (P06-CSloc, P06-3Dloc, SL2013+S40RTS) and combinations thereof (composite models). Depth-dependent scaling, based on mineral physics (Steinberger and Calderwood (2006)) and the ratio between compressional, shear and bulk sound velocities (Moulik and Ekström (2016)) were applied on the tomographic data and their influence was quantified. Spectral analysis, using spherical harmonics decomposition and re-synthesis, is performed on the synthetic models and benchmarked against satellite data in the same spectral range.

4.1 Effect of model resolution

CRUST1.0 consists of several compositional layers from surface topography to the Moho, yielding a resolution of 10m. Formatting the crustal data included projecting on an equidistant mesh. In the process, the largest achievable radial resolution of the data, in terms of file size, is 100m.

The model resolution of the CRUST1.0 model was sufficient to reach a model convergence. For benchmarking purposes, the CRUST1.0 model from ASPECT was quantitatively compared to the CRUST1.0 model from the spherical harmonics software. The smallest data residual was 8.44 mgal, which corresponds to $\sim 0.044\%$ of the crustal gravity signal. This misfit was obtained when either subtracting the mean of the full-spectrum spherical harmonics field and not re-sampling the gravity field from ASPECT or omitting the first spherical harmonics (d/o 1-179) and re-sampling the gravity field from ASPECT. The largest misfit values between the models mostly reside in continental regions and may originate in either the spherical harmonic approximation of the steep interfaces (e.g. continental roots or topography) or the resolution of the model in ASPECT. Although the misfit between the two crustal gravity fields can be quantified, it can not be constrained which method is qualitatively better.

ASPECT has proven to be a robust platform for crustal gravity modelling. Besides the successful benchmark with the spherical harmonics software, the influence of the mesh on the gravity signal is practically non-existent with an increase in quadrature points per cell. However, when a uniform density sphere is benchmarked against an analytical gravity vector an error of approximately $\sim 0.003\%$ of the gravity signal is caused by the inverse distance kernel of the volume integral in combination with the GLQ. The computational cost of gravity modelling in ASPECT in relatively high compared to the spherical harmonics software, however, considering ASPECT's potential of further development of the models (e.g. Stokes solver) this is taken for granted.

For larger models including the mantle, the largest hurdle in forward gravity modelling with ASPECT becomes the model resolution. The model resolution of the tomographic mantle models merely approximated data resolution. Due to computational limitations in memory the gravity signals of the tomographic models did not converge to a stable gravity field. Using a mesh of approximately 201 million cells, the maximum radial resolution achieved was 10.9 km whereas radial resolution of the data was 10 km. The error this imposes is difficult to quantify. The maximum data residual between the gravity fields of the radially best resolved two tomographic models (21.9 km versus 10.9 km) was 221 mgal for SL2013+S40RTS which corresponds to $\sim 0.037\%$ of the gravity signal. For P06-3Dloc and P06-CSloc this maximum

data residual was 69.68 mgal and 67.35 mgal respectively, which both correspond to $\sim 0.011\%$ of the gravitational signal. In addition, the lateral resolution of the tomography models had to be decreased from $0.5^\circ \times 0.5^\circ$ to $1^\circ \times 1^\circ$ in order to decrease the size of the data files.

Constructing composite models by merging crustal and tomographic data poses a trade-off between crustal and tomographic resolution. A compromise is chosen in which the models yielded a radial crustal resolution of 2.67 km and a radial mantle resolution of 21.93 km. This decrease in radial tomographic resolution means an error of at least $\sim 0.011 - 0.037\%$ of the mantle signal. Moreover, to limit the file size of the composite model, the crustal data resolution had to be reduced to 500 m. Figure 27 shows the difference between data sets with a radial resolution of 500m and 100m, the latter being the maximum achievable resolution. The largest errors this produced was 17.82 mgal, or $\sim 0.093\%$ of the crustal gravitational signal, and seems particularly concentrated on cratons (e.g. North American Craton, West African craton, Siberian craton). Therefore, it appears that a radial data resolution of 500 meters is not sufficient to properly resolve cratonic roots and the local topography of interfaces along which density contrasts exist.

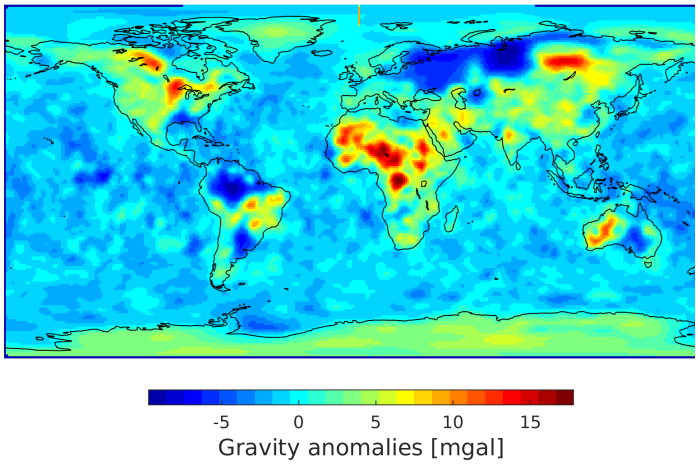

Figure 27: *The difference in gravity fields produced by CRUST1.0 for a 100 meter and 500 meter radial resolution.*

In an attempt to improve the radial resolution of the tomographic and composite models, a benchmark with a spherical chunk of uniform density was performed. Using the spherical chunk geometry in ASPECT comes with an option to increase radial resolution without increasing lateral resolution. This feature serves as alternative to the refinement through GMR, which always increases the model size with a factor 8. Potentially, the spherical chunk geometry would thus serve as a computationally more efficient alternative. However, because of edge effects, approximately 2.1% of the area of the gravity field retrieved the analytical value when wielding a 0.1% error margin. This deems the spherical chunk geometry an unreliable tool for gravity calculations.

The foremost improvement that would benefit forward gravity modelling in ASPECT is the addition of an option to modify the pre-refinement mesh, as is already available for the spherical chunk geometry. This way an improved radial resolution can be obtained without oversampling laterally. This would significantly reduce the size of the model and thus the computational cost. Incrementing the GMR with 1 increases the model size with a factor 8, however, the same radial increase in resolution without a lateral increase in resolution would increase the model size with a factor 2.

Also the option of a mesh consisting triangular icosahedron tesseroids, as opposed to an equiangular mesh, would reduce

the computational costs. A mesh of triangular icosahedron tesseroids, as used in Sebera et al. (2018), has similar sized cells per spherical shell. Cell size would not be dependent on their latitudinal position and re-sampling the gravity field would no longer be necessary.

Even after implementing mesh improvements, model resolution is expected to remain a problem. A potential solution, although computationally expensive, is subdividing the models into high-resolution spherical shells and performing gravity calculations separately from a consistent satellite height. Subsequently summing the separately calculated gravity fields could lead to a gravity field which utilizes all the data to the fullest extent. This, however, would disallow the use of the Stokes solver.

4.2 Data limitations

As shown in figure 23, the composite models suffer from unrealistic density jumps underneath the Moho in oceanic regions. This is due to, firstly, the merging of the data sets and the offset in their density values along the interface. Secondly, due to high-amplitude wave speed perturbations present in the shallow parts of the tomography data in combination with a low radial resolution of 10 km. Wave speed perturbations in the tomographic data sets sometimes exceed 30% in the upper 50 km. High-amplitude wave speeds perturbations are scaled to high-amplitude density perturbations. These density jumps are present in the upper part of the composite models and thus their gravitational signal is magnified in the gravity field. Essentially, the lithospheric resolution of the tomographic data does not suffice and higher-resolution data is required.

The density jumps underneath oceans can be artificially smoothed by, for instance, using a depth-weighted average for a chosen interval between the data sets. However, this would disregard the gravity contribution of the lithosphere-astenosphere boundary (LAB) and any heterogeneity within the lithosphere. The LAB beneath oceanic plates is a sharp boundary (Kawakatsu et al. (2009)) and the density contrast across the interface is in range of $20 - 100\text{kgm}^{-3}$ (Ebbing et al. (2006)). The LAB is expected to have a significant contribution on the gravity field.

To avoid relying on low-resolution tomographic data for the lithosphere and astenosphere when attempting to construct a composite model, a lithospheric model is needed. The effect of lithopsheric data gap on the gravity fields prohibits the investigation of deeper density perturbations. Options for models including the lithosphere are, for instance, LITHO1.0 (Pasyanos et al. (2014)) or LLNL-G3D-JPS (Simmons et al. (2015)).

LITHO1.0 (Pasyanos et al. (2014)) is a data set that extends into the lithosphere and the underlying astenosphere. LITHO1.0 has a resolution $\sim 1^\circ \times 1^\circ$ and is laterally parameterized by a spherical icosahedra tessellation with vertical nodes. LITHO1.0 utilizes above-mentioned crustal compilation CRUST1.0 as a starting point and supplements with lithospheric thicknesses of Pasyanos (2005) and tomographic upper mantle model LLNL-G3D (Simmons et al. (2012)). The LLNL-G3D-JPS Global Seismic Tomography model (Simmons et al. (2015)) was constructed through joint inversion of 3 million travel times generated by over 12,000 events and includes 56 high-resolution compositional layers from topography to CMB and includes both the Moho and the LAB.

4.3 Interpretation of gravity fields

Quantitatively comparing various gravity models is challenging because a gravity anomaly field is relative to the mean gravity field of this model. The satellite data set GOCO05c carries the gravity signal of the Earth's core (approx. 38% of the total $\vec{g}$) whereas the synthetic models don't. This prohibits a quantitative comparison between real-life and synthetic data. Therefore only the location and size of anomalies can be compared when comparing satellite data and synthetic data, not anomaly amplitudes.

4.3.1 Crustal gravity fields

The full-spectrum gravity field of CRUST1.0 (figure 16) shows clear patterns of positive gravity anomalies coinciding at with mid-ocean ridges, mantle upwelling underneath Iceland, the Pacific Islands and East-Africa. Subduction zones cannot be inferred consistently. Negative anomalies correlate to cratonic regions. The negative gravity signal from cratonic regions results from the continental roots with relatively low densities compared to the adjacent mantle material.

The long-wavelength gravity signature (d/o 1-4 and d/o 1-10) of CRUST1.0 (figure 26) does not correlate to GOCO05c in any spectral range. The long-wavelength gravity field of CRUST1.0 separates cratonic regions from oceanic regions. The gravity field in the spectrum d/o 1-4 shows a large-scale positive anomalous region in the central part of Eurasia and negative anomalous zones in the Pacific and Indian ocean. In the spectral range d/o 1-10, cratonic regions become pronounced through negative anomalous. Tenzer et al. (2015a) finds a correlation between medium and long wavelength gravity signal from CRUST1.0 and Moho topography. The model by Tenzer et al. (2015a) has been corrected for known anomalous crustal density structures (consolidated crust, topography, sediment, ice and bathymetry corrections). The long-wavelength signal produced by their model was dominated by the (relatively) smooth Moho geometry underneath oceanic regions and under basins with largely sedimentary accumulations. Adding short-wavelength signal to the gravitational signal led to a more detailed Moho geometry.
The gravity field as produced by this study (figure 26) will contain anomalous crustal density structure which, in turn, will contribute to medium-wavelength gravity signal. However, the long-wavelength gravity field might correlate to the first-order smooth Moho geometries.

4.3.2 Tomographic gravity fields

Interpretation of tomographic gravity fields is more challenging. The resolution and/or quality of the data in the upper parts of the tomographic models does not suffice. Known subduction zones surprisingly show negative gravity anomalies and cratonic regions show positive gravity anomalies. The LLSVP benchmark has shown that large-scale density perturbations from the lower mantle reside in the longest wavelengths of the gravitational signal (d/o 1-4). However, no consistent gravity anomalies are reproduced at the localities of the LLSVP's in this spectral range, either positive or negative. Moreover, the long wavelength signals from the tomographic data are not consistent among themselves. No information of the lower mantle density distribution can be extracted from the gravitational signal of these tomographic data sets.

Scaling the tomographic data with a depth-dependent conversion causes for a maximum deviation of $\sim 0.009 - 0.063\%$ of the gravitational signal. The effect of the scaling from Moulik and Ekström (2016) mostly resides in shallow part of the model, since the amplitude of the conversion function has a higher amplitude here with respect to the constant scaling

values. In contrast, the effect of the scaling from Steinberger and Calderwood (2006) resides in the upper mantle and emphasizes the gravitational signal of subduction zones and mantle upwelling. Both scaling techniques have significantly different conversion values for the lower mantle, the conversion from Steinberger and Calderwood (2006) being positive and the one from Moulik and Ekström (2016) being negative. This, however, does not clearly show in the gravity signatures. To conclude, only the relatively shallow conversion seems to affect the gravity signal.

When analyzing the long-wavelength gravity field of the individual tomographic models, the surface topography, Moho, LAB, transition zone, CMB ellipticity (Forte et al. (1995)) and CMB topography (Bowin (1986); Hager et al. (1985)) are not properly being taken into account. Interfaces with sharp density contrasts such as the Moho are able to produce gravity signals in the long-wavelength spectral range (Tenzer et al. (2015a)), therefore it cannot be excluded other large density contrasts will too. Especially the transition zone is likely to have a complex gravitational signal. The Clapeyron-slope of the chemical phase changes at 410, 520 and 660 km depth alter the topography of these discontinuities. The most prominent phase changes, being the 410 km and 660 km, yield a positive and negative Clapeyron slope respectively, meaning cold and warm temperature anomalies will deflect these discontinuities in an anti-correlating manner (Bina and Helffrich (1994)). Encountering colder material (subducted slabs), the 410 km discontinuity will deflect upwards and the 660 km will deflect downwards. Encountering hotter material (plume), the effect will be opposite. First order constraints on the amplitude of these deflections are up to 15-40 km (Fee and Dueker (2004); Helffrich (2000)) and the density contrasts at the discontinuities are $\sim 220\text{kgm}^{-3}$ for the 660km discontinuity and $\sim 125\text{kgm}^{-3}$ for the 410 discontinuity (Kennett et al. (1995)). Transition zone topography might offer an explanation for the gravitational signal of the tomographic data sets.

4.3.3 Composite gravity fields

Attempting to reconstruct (parts of) the Earth's gravitational field by merging the data has proved unsuccessful. Aforementioned, the lithospheric data gap corrupts the density distribution underneath oceans and creates a polarization between continental and oceanic gravity signals. No correlation with GOCO05c or geological features could be made in any spectral range.

Recommendations for model improvements are, firstly, incorporate a high resolution model of the LAB. Subsequently, topography of the discontinuities in the transition zone and topography and ellipticity of the CMB need to be constrained before the gravity signal of heterogeneity in the mantle can be isolated and analyzed.

5 Conclusions

One of the prominent limitations of geodynamical modelling of the Earth's mantle nowadays is the absence of a reliable density model. This research uses seismic tomography models to obtain a density profile through different forms of scaling. The gravity fields of these synthetic density profiles are calculated in order to compare to satellite data and thus test the density models. The gravity fields of CRUST1.0, three tomographic modles and combinations between them were calculated. Spectral filtering with spherical harmonics decomposition software was applied to investigate whether contributions from the Earth's mantle could be isolated.

ASPECT proved a reliable platform for forward gravity modelling. When benchmarked against spherical harmonics software, the data residual corresponded to $\sim 0.044\%$ of the gravitational signal. The largest hurdle in forward gravity modelling with ASPECT proved to be model and data resolution. Errors in the order of tens to hundreds of mgals were introduced by the Gauss-Legendre Quadrature, data resolution and model resolution. Due to computational limitations, the gravitational signals of the tomography models did not completely converge. The gravity signal of the tomographic model demonstrated surprising negative gravity anomalies at known subduction zones.

As a result of memory limitations, constructing the composite models (combinations of crustal and tomographic data) posed a trade-off between resolution in the crust and the mantle. The resolution and/or quality of the data in the upper part of the tomographic prohibited a smooth transition between the different data types, resulting in consistent underestimation of the density of oceanic lithosphere and astenosphere in the composite models.

The long-wavelength gravity field obtained from CRUST1.0 seems to be a first-order estimate of the smooth topography of the Moho, which is the discontinuity yielding the largest density contrast besides surface topography. The long-wavelength signal of the tomographic data did not allow for any correlation to lower mantle structure, nor were they consistent between themselves. Both the tomographic models sets and the composite models suffered from a lack of constraints and resolution on large density contrasts such as the lithosphere-astenosphere boundary, the transition zone and the CMB. In order to create synthetic gravity fields which resemble satellite data, these large density contrasts and their topography needs to be incorporated in the models before any information on the mantle's heterogeneity can be extracted from them.

6 Acknowledgements

I would like to thank dr. Bart Root, dr. Cedric Thieulot, prof. dr. Wim Spakman and dr. Ludovic Jeanniot for their expertise and guidance. I thank the Computational Infrastructure for Geodynamics (geodynamics.org) which is funded by the National Science Foundation under award EAR-0949446 and EAR-1550901 for supporting the development of ASPECT.

Also, I would like to thank the daily lunch crew and the coffee machine for their mental support.

References

Amaru, M. (2007). *Global travel time tomography with 3-D reference models*. PhD thesis, Utrecht University.

Andersen, O. B., Knudsen, P., and Berry, P. A. (2010). The dnsc08gra global marine gravity field from double retracked satellite altimetry. *Journal of Geodesy*, 84(3):191–199.

Antolik, M., Gu, Y. J., Ekström, G., and Dziewonski, A. M. (2003). J362d28: a new joint model of compressional and shear velocity in the earth's mantle. *Geophysical Journal International*, 153(2):443–466.

Bai, Y., Li, M., Wu, S., Dong, D., Gui, Z., Sheng, J., and Wang, Z. (2019). Upper mantle density modelling for large-scale moho gravity inversion: case study on the atlantic ocean. *Geophysical Journal International*, 216(3):2134–2147.

Bassin, C., L. G. and Masters, G. (2000). The current limits of resolution for surface wave tomography in north america. *EOS Trans AGU*, 81(F897). Available at https://igppweb.ucsd.edu/ gabi/crust2.html.

Bina, C. R. and Helffrich, G. (1994). Phase transition clapeyron slopes and transition zone seismic discontinuity topography. *Journal of Geophysical Research: Solid Earth*, 99(B8):15853–15860.

Bouman, J., Fiorot, S., Fuchs, M., Gruber, T., Schrama, E., Tscherning, C., Veicherts, M., and Visser, P. (2011). Goce gravitational gradients along the orbit. *Journal of Geodesy*, 85(11):791.

Bowin, C. (1986). Topography at the core-mantle boundary. *Geophysical Research Letters*, 13(13):1513–1516.

Chappell, A. and Kusznir, N. (2008). Three-dimensional gravity inversion for moho depth at rifted continental margins incorporating a lithosphere thermal gravity anomaly correction. *Geophysical Journal International*, 174(1):1–13.

Chertova, M., Geenen, T., van den Berg, A., and Spakman, W. (2012). Using open sidewalls for modelling self-consistent lithosphere subduction dynamics . *Solid Earth*, 3:313–326.

Deschamps, F., Snieder, R., and Trampert, J. (2001). The relative density-to-shear velocity scaling in the uppermost mantle. *Physics of the Earth and Planetary Interiors*, 124(3-4):193–212.

Dubey, C. and Tiwari, V. (2016). Computation of the gravity field and its gradient: Some applications. *Computers and Geosciences*, 88:83–96.

Dziewonski, A. and Anderson, D. (1981). Preliminary reference Earth model. *Phys. Earth. Planet. Inter.*, 25:297–356.

Dziewonski, A. M., Hager, B. H., and O'Connell, R. J. (1977). Large-scale heterogeneities in the lower mantle. *Journal of Geophysical Research*, 82(2):239–255.

Ebbing, J., Braitenberg, C., and Götze, H.-J. (2006). The lithospheric density structure of the eastern alps. *Tectonophysics*, 414(1-4):145–155.

Fecher, T., Pail, R., Gruber, T., Consortium, G., et al. (2017). Goco05c: a new combined gravity field model based on full normal equations and regionally varying weighting. *Surveys in geophysics*, 38(3):571–590.

Fee, D. and Dueker, K. (2004). Mantle transition zone topography and structure beneath the yellowstone hotspot. *Geophysical Research Letters*, 31(18).

Forsyth, D. W. (1985). Subsurface loading and estimates of the flexural rigidity of continental lithosphere. *Journal of Geophysical Research: Solid Earth*, 90(B14):12623–12632.

Forte, A. M., Mitrovica, J. X., and Woodward, R. L. (1995). Seismic-geodynamic determination of the origin of excess ellipticity of the core-mantle boundary. *Geophysical research letters*, 22(9):1013–1016.

Fullea, J., Rodríguez-González, J., Charco, M., Martinec, Z., Negredo, A., and Villaseñor, A. (2015). Perturbing effects of sub-lithospheric mass anomalies in goce gravity gradient and other gravity data modelling: Application to the atlantic-mediterranean transition zone. *International Journal of Applied Earth Observation and Geoinformation*, 35:54–69.

Garnero, E. and McNamara, A. (2008). Structure and Dynamics of Earth's Lower Mantle. *Science*, 320:626–628.

Ghosh, A., Thyagarajulu, G., and Steinberger, B. (2017). The importance of upper mantle heterogeneity in generating the indian ocean geoid low. *Geophysical Research Letters*, 44(19):9707–9715.

Guy, A., Holzrichter, N., and Ebbing, J. (2017). Moho depth model for the central asian orogenic belt from satellite gravity gradients. *Journal of Geophysical Research: Solid Earth*, 122(9):7388–7407.

Hager, B. H., Clayton, R. W., Richards, M. A., Comer, R. P., and Dziewonski, A. M. (1985). Lower mantle heterogeneity, dynamic topography and the geoid. *Nature*, 313(6003):541.

Heiskanen, W. A. and Moritz, H. (1967). Physical geodesy. *Bulletin Géodésique (1946-1975)*, 86(1):491–492.

Heister, T., Dannberg, J., Gassmöller, R., and Bangerth, W. (2017). High Accuracy Mantle Convection Simulation through Modern Numerical Methods. II: Realistic Models and Problems. *Geophy. J. Int.*, 210(2):833–851.

Helffrich, G. (2000). Topography of the transition zone seismic discontinuities. *Reviews of Geophysics*, 38(1):141–158.

Houser, C., Masters, G., Shearer, P., and Laske, G. (2008). Shear and compressional velocity models of the mantle from cluster analysis of long-period waveforms. *Geophysical Journal International*, 174(1):195–212.

Ishii, M. and Tromp, J. (1999). Normal-mode and free-air gravity constraints on lateral variations in velocity and density of earth's mantle. *Science*, 285(5431):1231–1236.

Kaban, M. K., Flóvenz, Ó. G., and Pálmason, G. (2002). Nature of the crust-mantle transition zone and the thermal state of the upper mantle beneath iceland from gravity modelling. *Geophysical Journal International*, 149(2):281–299.

Karato, S.-I. (1993). Importance of anelasticity in the interpretation of seismic tomography. *Geophys. Res. Lett.*, 20(15):1623–1626.

Karato, S.-i. and Karki, B. B. (2001). Origin of lateral variation of seismic wave velocities and density in the deep mantle. *Journal of Geophysical Research: Solid Earth*, 106(B10):21771–21783.

Kawakatsu, H., Kumar, P., Takei, Y., Shinohara, M., Kanazawa, T., Araki, E., and Suyehiro, K. (2009). Seismic evidence for sharp lithosphere-asthenosphere boundaries of oceanic plates. *Science*, 324(5926):499–502.

Kennett, B. and Engdahl, E. (1991). Traveltimes for global earthquake location and phase identification. *Geophysical Journal International*, 105(2):429–465.

Kennett, B., Widiyantoro, S., and Van Der Hilst, R. (1998). Joint seismic tomography for bulk sound and shear wave speed in the earth's mantle. *Journal of Geophysical Research: Solid Earth*, 103(B6):12469–12493.

Kennett, B. L., Engdahl, E., and Buland, R. (1995). Constraints on seismic velocities in the earth from traveltimes. *Geophysical Journal International*, 122(1):108–124.

Koelemeijer, P., Deuss, A., and Ritsema, J. (2017). Density structure of earth's lowermost mantle from stoneley mode splitting observations. *Nature communications*, 8:15241.

Koelemeijer, P., Ritsema, J., Deuss, A., and Van Heijst, H.-J. (2015). Sp12rts: a degree-12 model of shear-and compressional-wave velocity for earth's mantle. *Geophysical Journal International*, 204(2):1024–1039.

Kuhn, M. and Featherstone, W. (2005). Construction of a synthetic earth gravity model by forward gravity modelling. pages 350–355.

Kustowski, B., Ekström, G., and Dziewoński, A. (2008). Anisotropic shear-wave velocity structure of the earth's mantle: A global model. *Journal of Geophysical Research: Solid Earth*, 113(B6).

Laske, G. and Master, T. (1997). A global digital map of sediment thickness. *EOS Trans. AGU*, 78(F483). Available at http://igppweb.ucsd. edu/ gabi/sediment.html.

Laske, G., Masters, G., Ma, Z., and Pasyanos, M. (2013). Update on crust1. 0—a 1-degree global model of earth's crust. 15:2658.

Masters, G., Laske, G., Bolton, H., and Dziewonski, A. (2000). The relative behavior of shear velocity, bulk sound speed, and compressional velocity in the mantle: Implications for chemical and thermal structure. *Earth's deep interior: mineral physics and tomography from the atomic to the global scale*, pages 63–87.

Moulik, P. and Ekström, G. (2016). The relationships between large-scale variations in shear velocity, density, and compressional velocity in the Earth's mantle. *J. Geophys. Res.*, 121:doi:10.1002/2015JB012679.

Müller, R. D., Sdrolias, M., Gaina, C., and Roest, W. R. (2008). Age, spreading rates, and spreading asymmetry of the world's ocean crust. *Geochemistry, Geophysics, Geosystems*, 9(4).

Novák, P. and Grafarend, E. (2006). The effect of topographical and atmospheric masses on spaceborne gravimetric and gradiometric data. *Studia geophysica et geodaetica*, 50(4):549–582.

Oruç, B. and Sönmez, T. (2017). The rheological structure of the lithosphere in the eastern marmara region, turkey. *Journal of Asian Earth Sciences*, 139:183–191.

Pail, R., Fecher, T., Murböck, M., Rexer, M., Stetter, M., Gruber, T., and Stummer, C. (2013). Impact of goce level 1b data reprocessing on goce-only and combined gravity field models. *Studia Geophysica et Geodaetica*, 57(2):155–173.

Panning, M. and Romanowicz, B. (2006). A three-dimensional radially anisotropic model of shear velocity in the whole mantle. *Geophysical Journal International*, 167(1):361–379.

Pasyanos, M., Masters, T., Laske, G., and Ma, Z. (2014). Litho1.0: An updated crust and lithospheric model of the earth. *J. Geophys. Res.*, 119.

Pasyanos, M. E. (2005). A variable resolution surface wave dispersion study of eurasia, north africa, and surrounding regions. *Journal of Geophysical Research: Solid Earth*, 110(B12).

Resovsky, J. and Trampert, J. (2003). Using probabilistic seismic tomography to test mantle velocity–density relationships. *Earth and Planetary Science Letters*, 215(1-2):121–134.

Ritsema, J., Deuss, A., van Heijst, H., and Woodhouse, J. (2011). S40rts: a degree-40 shear- velocity model for the mantle from new rayleigh wave dispersio n, teleseismic traveltime and normal-mode splitting function measurements. *Geophy. J. Int.*, 184:1223–1236.

Ritsema, J., Ni, S., Helmberger, D. V., and Crotwell, H. P. (1998). Evidence for strong shear velocity reductions and velocity gradients in the lower mantle beneath africa. *Geophysical Research Letters*, 25(23):4245–4248.

Ritsema, J., van Heijst, H. J., and Woodhouse, J. H. (1999). Complex shear wave velocity structure imaged beneath africa and iceland. *Science*, 286(5446):1925–1928.

Ritzwoller, M., Shapiro, N., Levshin, A., Bergman, E., and Engdahl, E. (2003). Ability of a global three-dimensional model to locate regional events. *Journal of Geophysical Research: Solid Earth*, 108(B7).

Root, B., Novák, P., Dirkx, D., Kaban, M., van der Wal, W., and Vermeersen, L. (2016). On a spectral method for forward gravity field modelling. *Journal of Geodynamics*, 97:22–30.

Schaeffer, A. and Lebedev, S. (2013). Global shear speed structure of the upper mantle and transition zone. *Geophysical Journal International*, 194(1):417–449.

Sebera, J., Haagmans, R., Floberghagen, R., and Ebbing, J. (2018). Gravity spectra from the density distribution of earth's uppermost 435 km. *Surveys in Geophysics*, 39(2):227–244.

Simmons, N., Myers, S., Johannesson, G., Matzel, E., and Grand, S. P. (2015). Evidence for long-lived subduction of an ancient tectonic plate beneath the southern indian ocean. *Geophysical Research Letters*, 42(21):9270–9278.

Simmons, N. A., Forte, A. M., Boschi, L., and Grand, S. P. (2010). Gypsum: A joint tomographic model of mantle density and seismic wave speeds. *Journal of Geophysical Research: Solid Earth*, 115(B12).

Simmons, N. A., Forte, A. M., and Grand, S. P. (2009). Joint seismic, geodynamic and mineral physical constraints on three-dimensional mantle heterogeneity: Implications for the relative importance of thermal versus compositional heterogeneity. *Geophysical Journal International*, 177(3):1284–1304.

Simmons, N. A., Myers, S. C., Johannesson, G., and Matzel, E. (2012). Llnl-g3dv3: Global p wave tomography model for improved regional and teleseismic travel time prediction. *Journal of Geophysical Research: Solid Earth*, 117(B10).

Simons, F. J., Zuber, M. T., and Korenaga, J. (2000). Isostatic response of the australian lithosphere: Estimation of effective elastic thickness and anisotropy using multitaper spectral analysis. *Journal of Geophysical Research: Solid Earth*, 105(B8):19163–19184.

Sobolev, S. V., Zeyen, H., Granet, M., Achauer, U., Bauer, C., Werling, F., Altherr, R., and Fuchs, K. (1997). Upper mantle temperatures and lithosphere-asthenosphere system beneath the french massif central constrained by seismic, gravity, petrologic and thermal observations. *Tectonophysics*, 275(1-3):143–164.

Steinberger, B. and Calderwood, A. (2006). Models of large-scale viscous flow in the Earth's mantle with constraints from mineral physics and surface observations. *Geophy. J. Int.*, 167:1461–1481.

Su, W.-j. and Dziewonski, A. M. (1997). Simultaneous inversion for 3-d variations in shear and bulk velocity in the mantle. *Physics of the Earth and Planetary Interiors*, 100(1-4):135–156.

Tenzer, R., Chen, W., Tsoulis, D., Bagherbandi, M., Sjöberg, L. E., Novák, P., and Jin, S. (2015a). Analysis of the refined crust1. 0 crustal model and its gravity field. *Surveys in geophysics*, 36(1):139–165.

Tenzer, R., Chen, W., and Ye, Z. (2015b). Empirical model of the gravitational field generated by the oceanic lithosphere. *Advances in Space Research*, 55(1):72–82.

Trampert, J. (1998). Global seismic tomography: the inverse problem and beyond. *Inverse Problems*, 14(3):371.

Van der Hilst, R. D., Widiyantoro, S., and Engdahl, E. (1997). Evidence for deep mantle circulation from global tomography. *Nature*, 386(6625):578.

van der Meer, D. G., van Hinsbergen, D. J., and Spakman, W. (2018). Atlas of the underworld: Slab remnants in the mantle, their sinking history, and a new outlook on lower mantle viscosity. *Tectonophysics*, 723:309–448.

Xu, X., Zhao, Y., Reubelt, T., and Tenzer, R. (2017). A goce only gravity model gosg01s and the validation of goce related satellite gravity models. *Geodesy and Geodynamics*, 8(4):260–272.

Zhou, X. (2008). 2D vector gravity potential and line integrals for the gravity anomaly caused by a 2D mass of depth-dependent density contrast. *Geophysics*, 73(6):143–150.

7 Appendices

7.1 Computational statistics

ASPECT was run on a device called Eejit, which has 80 compute nodes, each having two AMD EPYC 7451 24-Core Processors and 256 GB memory. Between 20-25 of these nodes were usually used. The largest models, being the composite models, used 25 nodes and took ∼12 hours with 2,666,399,286 degrees of freedom.
The spherical harmonics software were run on a single processor, being Intel(R) Core(TM) i7-7700HQ. Computing the gravity field of CRUST1.0 took approximately 15 seconds.

7.2 GOCO05c vs. CRUST1.0+P06-3Dloc

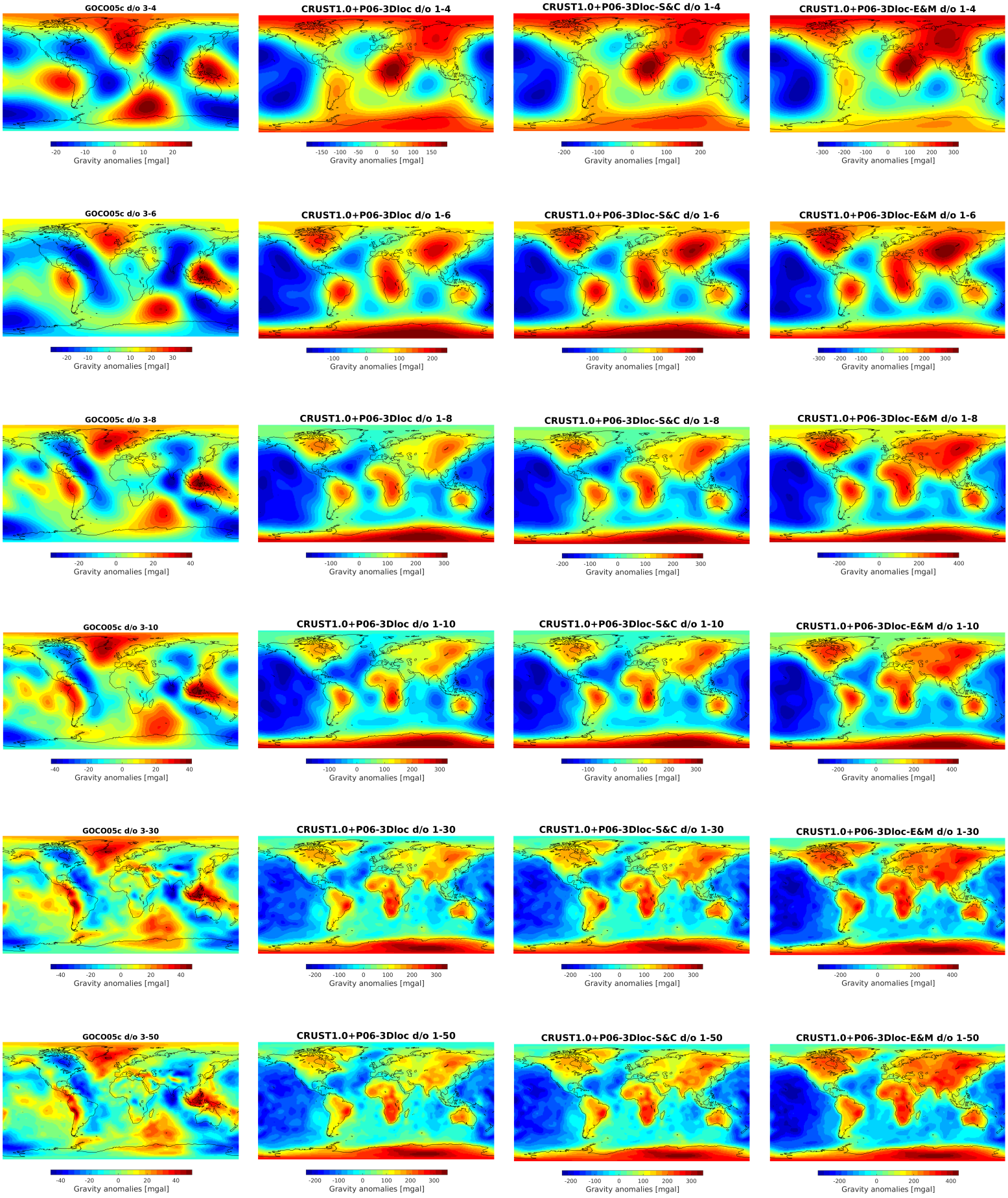

Figure 28: *GOCO05c (first column) and CRUST1.0+P06-3Dloc with constant scaling (2nd column), with the scaling of Steinberger and Calderwood (2006) (third column) and with the scaling of Moulik and Ekström (2016) (fourth column) - in various spectral ranges.*

7.3 GOCO05c vs. CRUST1.0+P06-CSloc

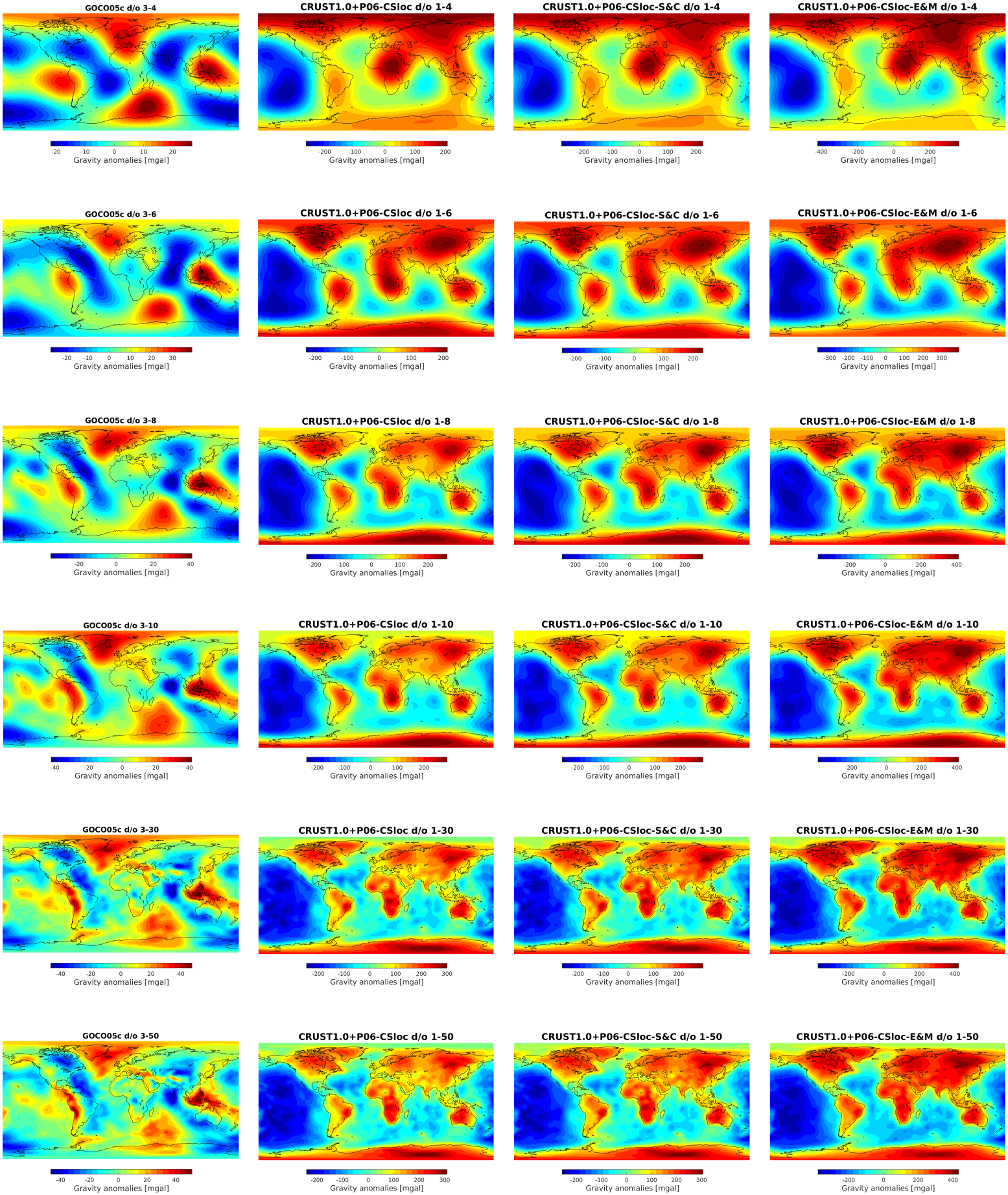

Figure 29: *GOCO05c (first column) and CRUST1.0+P06-CSloc with constant scaling (2nd column), with the scaling of Steinberger and Calderwood (2006) (third column) and with the scaling of Moulik and Ekström (2016) (fourth column) - in various spectral ranges.*

7.4 GOCO05c vs. CRUST1.0+SL2013+S40RTS

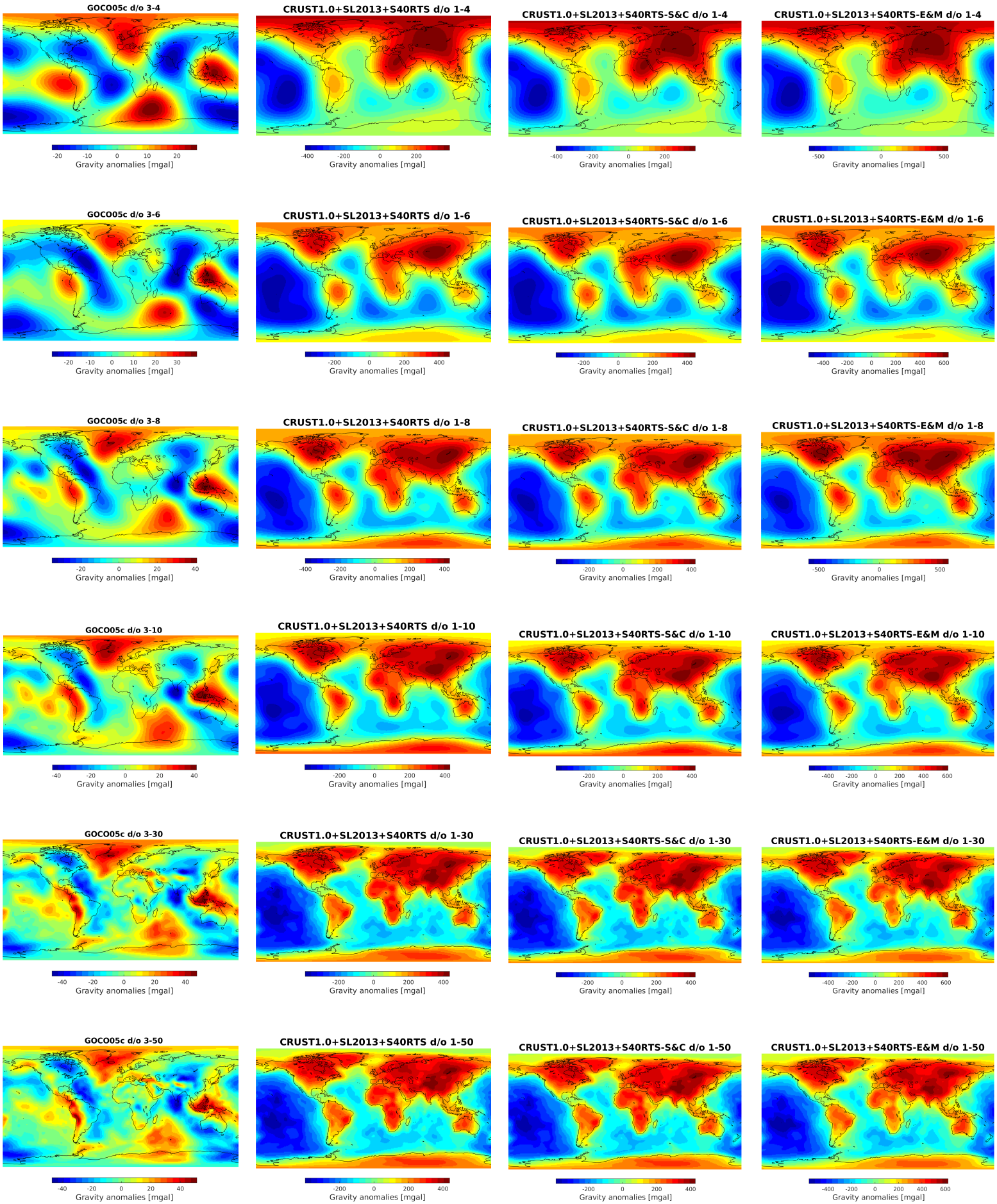

Figure 30: *GOCO05c (first column) and CRUST1.0+SL2013+S40RTS with constant scaling (2nd column), with the scaling of Steinberger and Calderwood (2006) (third column) and with the scaling of Moulik and Ekström (2016) (fourth column) - in various spectral ranges.*